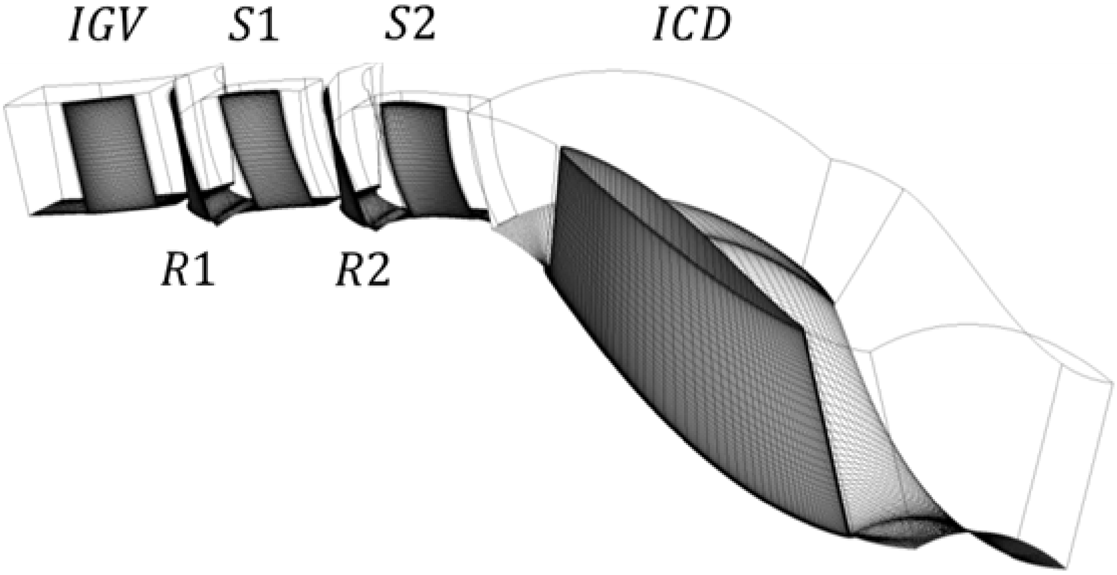

Numerical modeling of laminar-turbulent transition in an interconnecting compressor duct

BLANCA GONZÁLEZ LOZANO

DEPARTMENT OF MECHANICS AND MARITIME SCIENCES

CHALMERS UNIVERSITY OF TECHNOLOGY

Gothenburg, Sweden 2022

www.chalmers.se

Master's thesis 2022

Numerical modeling of laminar-turbulent transition in an interconnecting compressor duct

Blanca González Lozano

Department of Mechanics and Maritime Sciences
Division of Fluid Dynamics
Chalmers University of Technology
Gothenburg, Sweden 2022

Numerical modeling of laminar-turbulent transition in an interconnecting compressor duct
BLANCA GONZÁLEZ LOZANO

Supervisor: Alexandre Capitao Patrao, Mechanics and Maritime Sciences
Examiner: Carlos Xisto, Mechanics and Maritime Sciences

Master's Thesis 2022
Department of Mechanics and Maritime Sciences
Division of Fluid Dynamics
Chalmers University of Technology
SE-412 96 Gothenburg
Telephone +46 31 772 1000

Cover: ENABLEH2 compressor geometry

Typeset in LaTeX
Printed by Chalmers Reproservice
Gothenburg, Sweden 2022

Numerical modeling of laminar-turbulent transition in an interconnecting compressor duct
BLANCA GONZÁLEZ LOZANO
Department of Mechanics and Maritime Sciences
Chalmers University of Technology

Abstract

With the purpose of meeting the challenging environmental targets set by the European Union (EU) in 2019, new sustainable fuels need to be inserted in the aviation industry [1]. Hydrogen stands out to be a promising candidate to be adapted into the aviation fuel mix due to its CO_2-free combustion, and higher energy density compared to kerosene.Nevertheless, due to its poor volumetric energy density, hydrogen (H_2) storage requires higher aircraft volumes that leads to poorer aerodynamic performances. Liquid hydrogen (LH_2) offers a two-fold increase in volumetric energy density to that of highly compressed H_2. This makes LH_2 a prime candidate for aviation since it decreases the required volume by half. However, to fulfil the low weight requirements set by aircraft, the liquid hydrogen must be stored at cryogenic temperatures at a pressure close to or slighter higher than ambient. As a consequence, adequate tank insulation technology needs to be developed. In addition, with the goal of increasing the effective heating value of hydrogen, heat exchanger technology must be included in the fuel distribution system. Up to the present time, different heat exchanger technologies placed in the vicinity of the engine have been investigated [2]

This project focuses on how to model the vane surfaces of an Intermediate Compressor Duct (ICD) using CFD for the purpose of intercooling to support and prepare for future validation work using the Chalmers low pressure compressor rig. This study will analyze the behavior of different CFD transition models in the prediction of laminar-turbulent transition, mesh dependency, impact of wall temperature as well as theoretical validation of the results.

CFD simulations using the Gamma-Theta and Intermittency transition models showed very similar results and highlighted the need of well-refined computational grids in order to reach mesh independence for pressure loss, heat flow, and transition onset and duration. A parametric study where the vane wall temperatures were decreased showed that transition was delayed for decreasing wall temperatures and that the length of the transition zone decreased as well. Moreover, flat plate correlations employed to validate the results turned out to not be accurate enough in the prediction of transition.

Keywords: Turbulence transition model, intermediate compressor duct (ICD), heat exchanger, hydrogen.

Acknowledgements

First of all, I would like to extend my utmost gratitude to my supervisors, Alexandre Capitao and Carlos Xisto, for introducing and guiding me in the passionate world of CFD. Thank you for the trust you have placed in me during these months and for letting me work in such a fun and inspiring environment. Also, I really appreciate the continuous and motivating feedback you gave me throughout the thesis.

I am also very grateful towards the entire Fluid-Dynamics division for welcoming me so well since the beginning and for making me feel part of this little family. Also, thanks to Chalmers University for this amazing year. Once a chalmerist, always a chalmerist!

In addition, thank you to the the Chalmers Centre for Computational Science and Engineering (C3SE) because without it´s support and computational infrastructure, this project could not have been developed.

To my friends, the ones I had before and after coming to Sweden, for everything we have shared and we will share together. Also to Andres, for always being by my side through thick and thin.

Finally, a special heart-felt thank you to my parents for their enduring support and unconditional belief in me, and to the person who I have as a reference in my life, my sister, for always pushing me to be my best self.

Blanca González Lozano, Gothenburg, June 2022

List of Acronyms

Below is the list of acronyms that have been used throughout this thesis listed in alphabetical order:

ACARE	Advisory Council for Aeronautics Research in Europe
Δh_0	Change in total enthalpy from inlet to outlet for the core air
Δp_0	Change in total pressure from inlet to outlet for the core air
CC	Combustion Chamber
CFD	Computational Fluid Dynamics
Re_c	Critical Reynolds Number
y^+	Dimensionless first node height
μ	Dynamic Viscosity
EU	European Union
T_∞	Freestream Temperature (K)
u_∞	Freestream Velocity $[m/s^2]$
GHG	Green House Gas
h	Heat transfer coefficient
HPC	High Pressure Compressor
HPT	High Pressure Turbine
IGV	Inlet Guide Vane
IC	Intercooling
ICD	Intermediate Compressor Duct
IPC	Intermediate Pressure Compressor
LH_2	Liquid Hydrogen
LPC	Low Pressure Compressor
LPT	Low Pressure Turbine
N_{cells}	Number of cells in the mesh
Nu	Nusselt Number
OGV	Outlet Guide Vane
U	Overall heat transfer coefficient $[W/m^2K]$
Pr	Prandtl Number
PC	Precooling
r	Pressure Ratio

REC	Recuperator
Re	Reynolds Number
R1	Rotor 1
R2	Rotor 2
S1	Stator 1
q_x''	Surface heat flux $[W/m^2]$
T_s	Surface Temperature
k	Thermal conductivity $[W/mK]$
R_{tot}''	Thermal resistance per unit area $[m^2K/W]$
UWH	Uniform Wall Heat Flux
UWT	Uniform Wall Temperature
q_{vane}	Vane heat flow $[W]$
VINK	Virtual Integrated Compressor Demonstrator
t	Wall thickness $[m]$

Contents

List of Figures

List of Tables

1

Introduction

Since the European Green Deal was published in December 2019, the European Union (EU) has the goal of achieving zero net emissions by 2050 as well as reducing Green House Gas (GHG) emissions by at least 55% by 2030, compared to 1990 levels [1]. For the purpose of achieving that challenging goal, emissions need to be reduced in all European industries. In particular, changes in transport and electricity production sectors must be introduced as they have the largest reduction potential amounting to 31% and 30% of the total CO_2 emissions in the EU, respectively [3].

Within the direct GHG emissions produced in Europe by transportation in 2017, 13.9% came from aviation, accounting for 3.8% of the total CO_2 emissions. Furthermore, aviation does impact the climate through the release of other emissions such as nitrogen oxides, water vapour, sulphate, and soot particles. This along with the fact that the air traffic is continuously growing, leads to the risk of having, by 2050, the triple of emissions than in 2015 [4]. In order to avoid so, new sustainable carbon free fuels as well as new technology needs to be employed and developed.

Fossil-based fuels have commonly been used in aircraft engines. However, due to the strict regulations set on fossil fuels such as taxes on its use [5] as well as because of their relevant polluting effect and their finite supply, widespread studies about new and alternative fuels have been developed with the goal of eliminating CO_2 emissions [6].

In the case of the aviation industry, the emission targets to be achieved by 2050 were established by the **ACARE** (Advisory Council for Aeronautics Research in Europe) which stated that a 75% and 90% reduction in CO_2 and NO_x emissions, respectively, should be achieved [7]. In order to overcome with both limitations, the fuel that stands out to be the most suitable option is liquid hydrogen (LH_2), due to its CO_2 free combustion, and higher energy density (2.6 times higher compared to kerosene) [8]. The main benefit on the use of liquid hydrogen as the main aircraft fuel is its decreased environmental impact. Compared to other fuels, liquid hydrogen eliminates CO_2, CO, soot, sulphur, and unburnt hydrocarbons emissions. Additionally, the increased flammability limits of hydrogen allow for stable leaner combustion, hence reducing flame temperatures and NO_x emissions [9].

Nevertheless, LH_2 has the need of being stored at cryogenic temperatures (-253°C) which leads to the need of having adequate tanks for minimum boil-off and fuel lines with adequate insulation for safe operation without vapor lock. [2]. The fuel also requires an integrated heat management system in order to inject the fuel at adequate temperatures in the combustion chamber [7].

Thermal management is the process by which the fuel absorbs the excess heat generated by the different components and systems of the engine as it passes through them. An example of this is shown in Figure 1 which features precooling, intercooling, and recuperation. Precooling and intercooling decreases compressor work, while recuperation absorbs excess thermal energy in the exhaust [7]. As a result of this, an overall improvement of the engine performance, as well as an enhancement on the thermal efficiency of the engine can be reached [8]. When using cryogenic hydrogen as a coolant, the offered cooling capacity plays a really important role as it opens the door to improving both the engine performance as well as the life expectancy of the different components [9]. As a result, heat exchanger design in hydrogen aeroengines must be carried out carefully [10, 11].

Up to present time, widespread types of heat exchangers such as shell and tube, crossflow or double pipe have been developed. However, its complexity inside engine architecture makes its use and development limited. In comparison, using the intermediate compressor ducts and the turbine outlet guide vanes as heat exchangers would not only allow the hydrogen´s temperature to increase due to the thermal energy expelled by the surfaces on both parts of the engine, but it would also be an engine design that could be truly patented and developed by manufacturers. This revolutionary design was proposed and tested by NASA in 1978. Since then, different studies have been carried out in order to analyze the most optimum compressor and turbine nozzle geometry that leads to lower heat losses, thus, greater heat transfer [12].

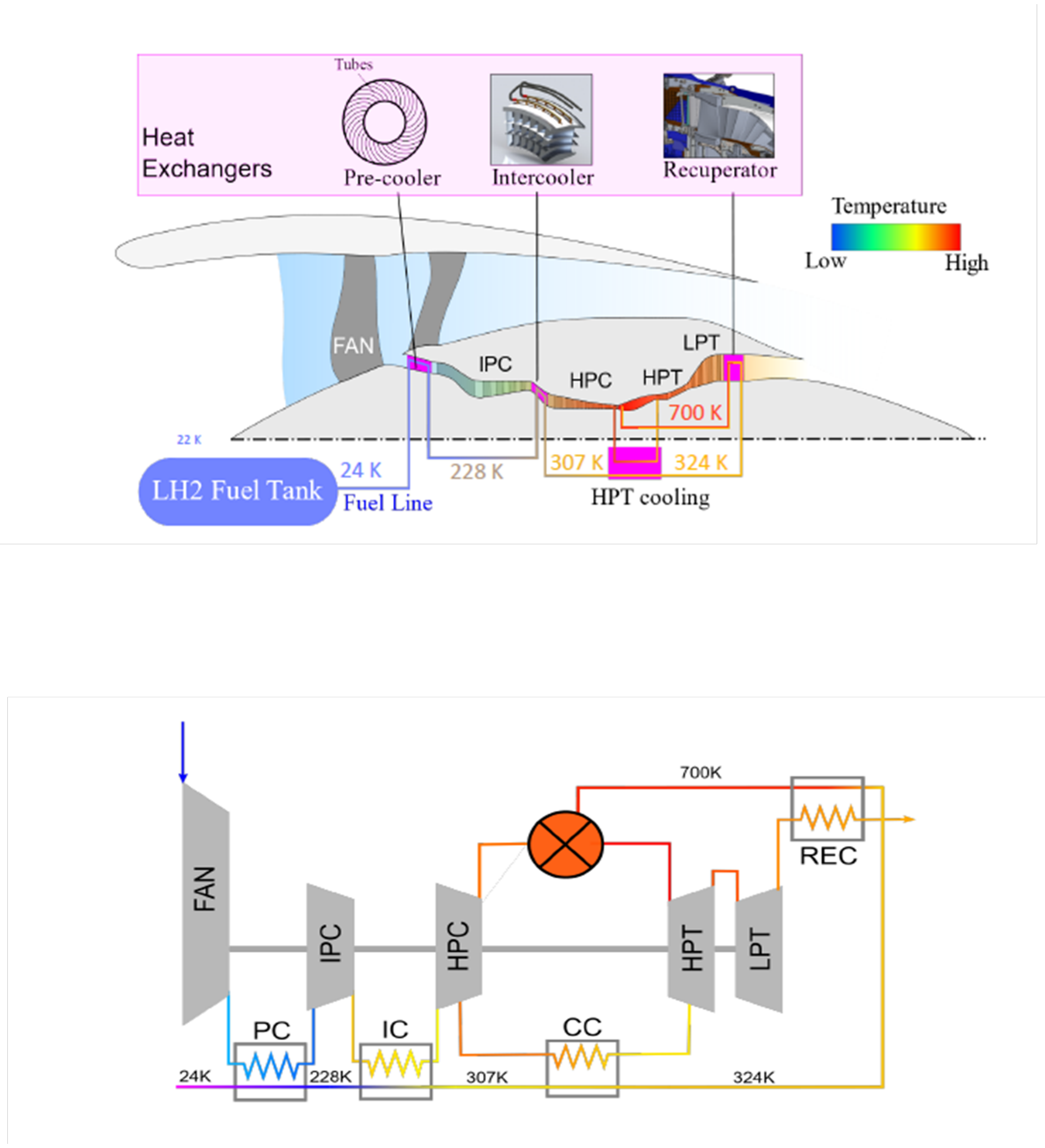

Figure 1.1: Cross sectional meridional view of a turbofan engine in which different locations for core cooling using liquid hydrogen are shown. The used fuel, LH_2 (liquid hydrogen), is stored at its boiling point in the fuel tank. The LH_2 temperature is progressively increased as a result of the fuel flow across the different core installed heat exchangers. IPC: Intermediate-pressure compressor; HPC: High pressure compressor; HPT- High-pressure turbine; LPT-Low pressure turbine [13].

2

Theoretical Framework

2.1 Introduction to Heat Transfer

With the purpose of better understanding this project, during the following pages a small brushstroke will be given on the most general and basic concepts about fluid dynamics and heat transfer.

Heat Transfer can be defined as thermal energy in transfer on account of a temperature difference in a medium or between media. There are three fundamental methods by which this heat exchange can occur (Figure 2.1):

Conduction, term used to define the heat transfer across the medium when a temperature gradient exists in a stationary medium such as a solid or a fluid [14].

Convection, instead, refers to heat transfer between a moving fluid and a surface when their temperatures differ.

Thermal Radiation is the last mode of heat transfer and occurs when surfaces of finite temperature emit energy in the form of an electromagnetic waves.

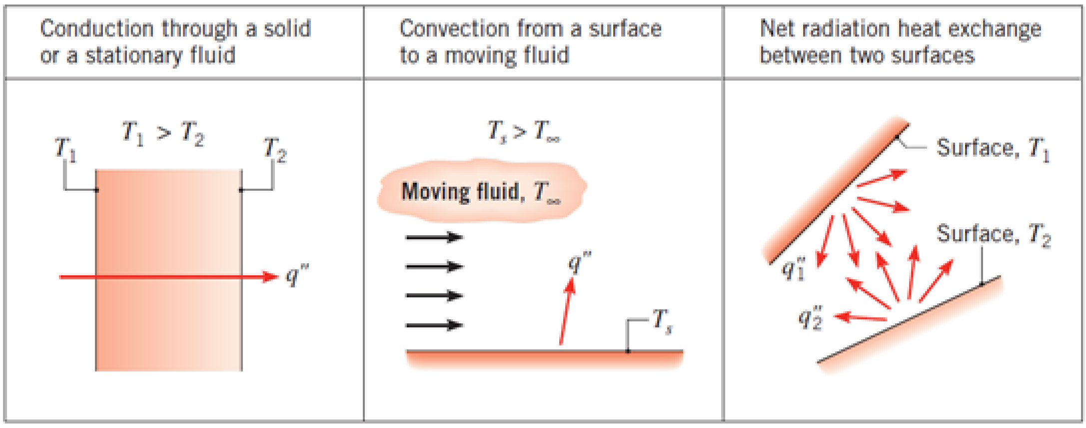

Figure 2.1: Scheme of the three different heat transfer modes. From left to right: conduction, convection and thermal radiation. [14]

2.1.1 Thermal Radiation

Thermal radiation is the energy emitted in form of electromagnetic waves by either solid surfaces, liquids or gases which are at nonzero temperature. In comparison to the other two ways of heat transfer, conduction and convection, thermal radiation does not require the presence of a material medium to transfer the energy [14].

In the case of thermal radiation, the heat flux (E) emitted by a surface is given by the *Stefan Boltzmann* law:

$$E = \epsilon\sigma T_s^4 \tag{2.1}$$

Where T_s (K) is the absolute temperature of the surface, σ is the *Stefan Boltzmann* constant ($\sigma = 5.67 \times 10^{-8}\, W/m^2 * K^4$) and ϵ, known as emissivity, and whose value is in the range $0 < \epsilon < 1$, is a radiative property of the surface that provides a measure of how efficiently the energy is emitted in comparison to a blackbody [14].

Thermal radiation plays an important role in a wide range of engineering applications, especially in those that take place at elevated temperatures. In the case of conduction and convection, (Section 2.1.2 and 2.1.3) the energy transfer between two bodies depends roughly on the temperature difference between them. However, in the case of thermal radiation, the heat transfer between two distant bodies is a function of the difference between the fourth power of their absolute temperatures [15]. Taking this into account as well as the fact that low temperatures are employed in this project, radiation can be considered as a negligible phenomenon in comparison with convection and conduction, reason why no extended study is developed around this third way of heat transfer.

2.1.2 Conduction

Conduction can be defined as the transfer of energy from the more energetic particles, thus, higher temperatures, to the less energetic particles of a medium as a result of interactions, such as collisions, between them.

Heat transfer processes employ rate equations in order to estimate the amount of energy being transferred per unit time.

In the case of conduction, the rate equation is known as ***Fourier's law***:

$$q'' = -k\nabla T = -k\left(\mathbf{i}\frac{\partial T}{\partial x} + \mathbf{j}\frac{\partial T}{\partial y} + \mathbf{k}\frac{\partial T}{\partial z}\right) \tag{2.2}$$

However, the previous rate equation can be easily simplified in the case of having heat transfer in only one direction, converting it from a vector equation into a scalar equation:

$$q''_x = -k\frac{dT}{dx} \tag{2.3}$$

The heat flux, q''_x, expressed in $\frac{W}{m^2}$, represents the amount of heat transferred per unit area perpendicular to the heat transfer direction.

The parameter k, known as thermal conductivity, is a characteristic property of each material that quantifies how well the heat is transferred.

The temperature gradient, $\frac{dT}{dx}$, expresses how temperature changes along the heat transfer direction. In order to represent that the heat is being transferred in the direction of decreasing temperatures, which is opposite to the gradient direction, it is necessary to include a minus sign in the equation (-)

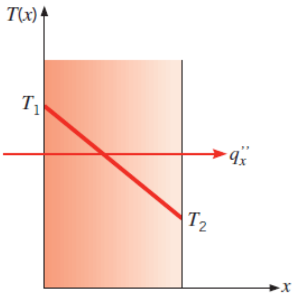

Figure 2.2: Heat direction and temperature gradient in one dimension [14].

2.1.3 Convection

In **convection**, the energy is transferred by advection (macroscopic motion of the fluid) and diffusion (random molecular motion) as a result of the interaction between a surface and a moving fluid whose temperatures differ. However, diffusion energy transfer is the main mechanism near the surface and the only existing one when reaching the surface (y=0) due to its low or even zero velocities.

There are different types of convection, being *natural* and *forced* convection the most relevant ones. Whereas natural convection is related to variations in density due to changes in temperature (buoyancy forces), forced convection responds to the process caused by external forces such as pumps or fans.

The rate equation in convection heat transfer is known as **Newton´s law of cooling**:

$$q'' = h\left(T_s - T_\infty\right) \tag{2.4}$$

Where T_s (K) is the surface temperature, T_∞ (K) is the free stream fluid temperature, and **h** $(W/(m^2 * K))$ is a parameter named convection heat transfer coefficient which depends on mainly all conditions in the boundary layer such as nature of the fluid motion, thermodynamic and transport properties as well as the employed geometry.

2.1.3.1 Velocity Boundary Layer

In the flow of a fluid over a surface, the **velocity boundary layer** is known as the fluid part which becomes slower as a result of its contact with the surface.

As a result of viscosity, when a particle strokes a surface, its velocity becomes zero. This process causes the following incoming particles to hinder until no disturbance exists and the freestream velocity (U_∞) is obtained. The retard in the fluid motion is produced as a result of shear stresses (τ) applied in parallel planes to the fluid. Furthermore, the boundary layer thickness (δ) is known as the y value in which the velocity is 99% the freestream velocity $(u = 0.99u_\infty)$.

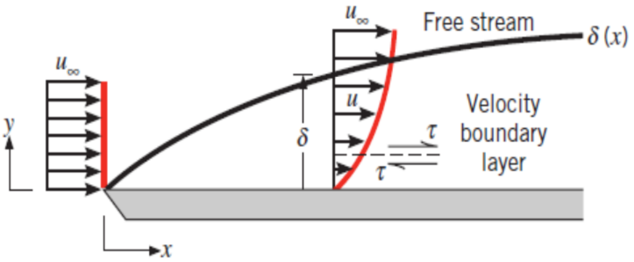

Figure 2.3: Velocity boundary layer over a flat pate [14].

Moreover, 3 different regions, each of them with different fluid behaviour, can be distinguished in the boundary layer. These are: the laminar, transition and turbulent regions (Figure 2.4)

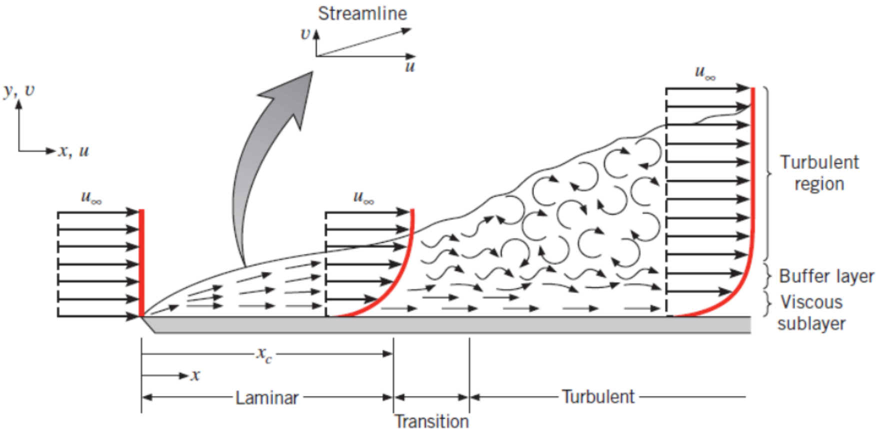

Figure 2.4: Velocity boundary layer development on a flat pate [14].

Laminar regime is characterized by the smoothness, uniformity and high ordered flow. In this region, the fluid moves horizontally in layers with minimum mixing between them. In contrast, turbulent region is characterized by the chaotic flow pattern as well as by its greatly irregular and random fluid motion caused by the appearance of vortices known as streaks. In addition, the turbulent region can also present a viscous sub-layer with nearly laminar properties, an adjoining buffer layer in which diffusion and turbulent mixing co-exist, and a third zone in where mixing is dominant. The third an intermediate region, which will be further studied in section 2.2 is known as the transition region.

2.1.3.2 Yplus

As explained in Subsection 2.1.3.1, in fluid mechanics a boundary layer is known to be a layer of fluid near a bonding surface where the effect of viscosity is significant. This phenomenon is of great importance when analyzing the fluid flow over a surface.

In CFD, the analyzed fluid domain is solved by discretizing the entire domain into small volumes in which the continuity, momentum and energy equations are solved. In order to check that the numerical grid provides sufficient resolution to resolve the boundary layer adequately, the dimensionless parameter y^+ is employed. This parameter provides a relation between the friction velocity (u^+), the absolute distance from the wall (y) and the kinematic viscosity (ν) [16]:

$$y^+ = \frac{u^* y}{\nu} \tag{2.5}$$

$$u^* = \sqrt{\frac{\tau_w}{\rho}} \tag{2.6}$$

Where ρ is the fluid density and τ_w the wall shear. Moreover, as it can be seen in figure 2.5, depending on whether the flow is turbulent or laminar, different wall shear´s are reached.

However, depending on which turbulence model is used, different y^+ values are required to obtain the properly model on each of the different sub-layers over the near-wall region. The values required to obtain the desired accuracy for each of the labels are [16]:

Viscous Sub-layer: $0 < y^+ < 5$
Buffer Layer: $5 < y^+ < 30$
Internal Sub-Layer: $30 < y^+ < 200$

In the case of this project, where the two laminar-transition models explained in section 2.5.4.1 and 2.5.4.2 are used, it is necessary to have a value of $y^+ < 1$ in order to be able to resolve the boundary layer all the way toward the wall.

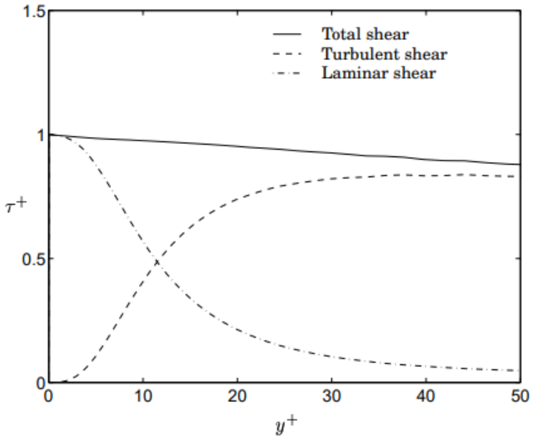

Figure 2.5: Laminar and turbulent shear in the near wall region [16].

2.1.3.3 Thermal Boundary Layer

As well as the velocity boundary layer arises due to a velocity difference, the **thermal boundary layer** appears as a result of the temperature difference between the fluid and the wall. In this case, hot particles exchange heat with those colder around them. As a result of this heat exchange process, a temperature gradient is developed which results in a thermal boundary layer thickness (δ_t) characterized by $\frac{T_s - T}{Ts - T_\infty} = 0.99$. (Figure 2.6)

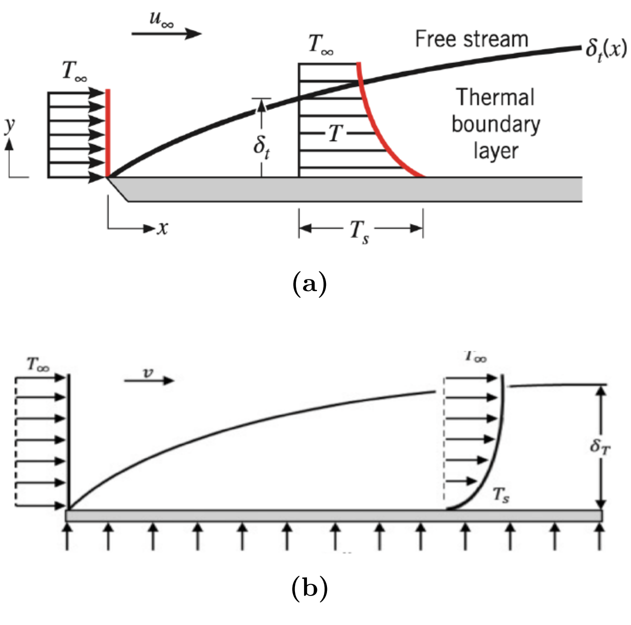

Figure 2.6: Thermal Boundary layer over a flat plate in two different cases: a) More temperature than the freestream´s. b) Less temperature than the freestream´s [14].

Moreover, just like in the velocity boundary layer, 3 different regions can be distinguished in the thermal boundary layer. In each region fluid properties and behaviour of the flow is different. For example, while in the transition region, the heat transfer coefficient presents a large variation, in the turbulent region this fluctuation is bigger due to the more agitation produced by the continuous exchange in heat and mass between the different turbulent layers .

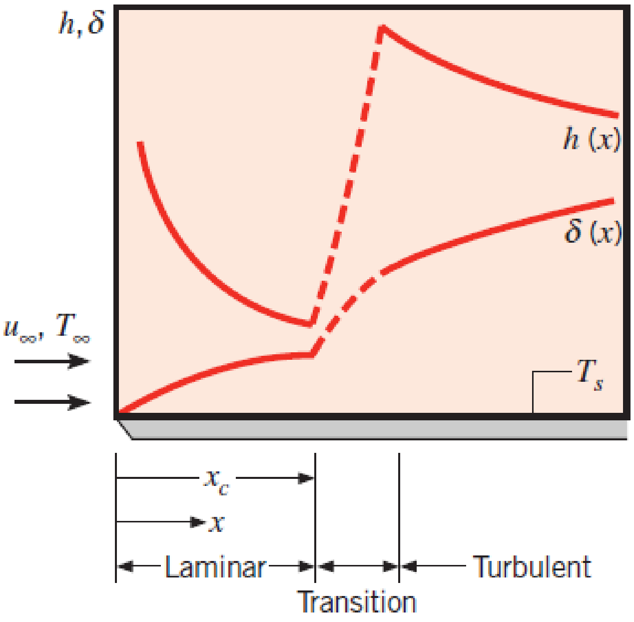

Figure 2.7: Heat transfer coefficient (h) variation with the boundary layer [14].

2.2 Laminar-Turbulent Transition

Predicting which flow regime is likely to be produced when working under different flow conditions is of great importance due to the big differences laminar and turbulent flows entails. To do so, it is important to study where transition starts. *Transition* also called *Onset of Turbulence*, is the multiple-stage process through which a laminar flow becomes turbulent [17].

Osborne Reynolds demonstrated the laminar-turbulent transition process through his famous experiment where he observed the motion of water flow at different flow rates by introducing dyed water into it. At low flow rates, he visualized that the stream of dyed water remained constant throughout the length of the tube. However, as the flow rate was increased up to a certain value, the dye diffused across the entire cross-section of the tube. In fact, it is through these experiments that he proposed a similarity criterion, which eventually became the Reynolds number [18].

The Reynolds number (2.6.1) is a non-dimensional parameter employed to predict whether the flow is laminar or turbulent by relating the inertial and viscous forces of the fluid. Moreover, the Reynolds number at which the transition to the turbulent regime occurs is defined as the *Critical Reynolds Number* and it´s value can significantly vary depending on the type of flow being analyzed.

To understand what causes transition it is important to study the concept of stability. Stable systems are defined as those that withstand disturbances and return to its original undisturbed state. In contrast, unstable systems are those that never return back to it´s original undisturbed state. From fluid dynamics point of view, a fluid is considered to be stable when absorbs and does not exhibit noticeable changes when external disturbances such as surface roughness anomalies or flow property variations are encountered. In the case of unstable fluid flows, any small disturbance applied on it turns out on noticeable flow variations, thus, the beginning of the the laminar-turbulent transition region begins [18].

The phenomenon of transition is dependent on many factors such as the surface roughness, the free stream turbulence intensity or the flow conditions. For example, in the case of boundary layer flows such as the flow over a solid surface, the primary instability/transition mechanism is trough the amplification of **Tollmien-Schlichting waves**. These waves, which get amplified and force the uniform boundary layer to transition to the three-dimensional turbulent, are two dimensional disturbances that travel in the mean flow direction [18].

The process by which the TS waves emerge and thereby eventual transition to turbulence starts, is characterized by having laminar flow at the leading edge until a location where the Reynolds number in the flow is lower than the *Critical Reynolds number*. Beyond this point, 2D TS waves emerge and start travelling downstream. These 2D waves rapidly become unstable taking the shape of three dimensional hairpin eddies which break down creating a cascade of turbulent eddies together.

As a result, turbulent spots are formed. The combination of these spots ends up on a fully turbulent region, thus, the end of the transition process. (Figure 2.8)

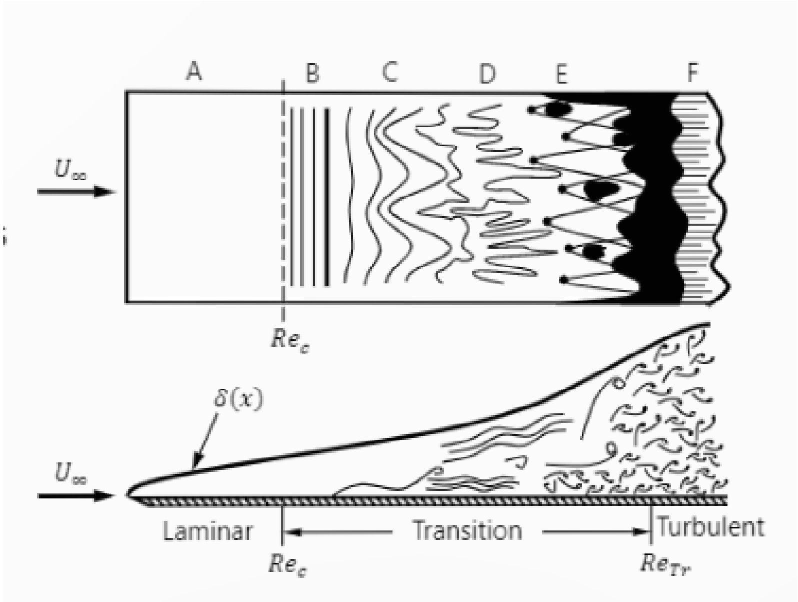

Figure 2.8: Transition process for a flat plate in where A is the laminar flow region, B the point from which 2D TS waves emerge, C the location in where 3D structures (vortices) are formed, D the point at which the vortices break down leading to the formation of turbulent spots, thus, the beginning of transition (E) until F, where transition ends and therefore fully turbulent flow begins[18].

However, in the case of free-shear layer flows, where fluids are moving at different velocities relative to each other, the instability mechanism that describes the transition process is in the form of vortical structures or ocean-like waves commonly referred as the *Kevin-Helmholtz Instability* [18].

Nowadays, numerical simulations are performed in order to identify the conditions at which the fluid flow starts transition. However, a few hundred years ago, scientists did not have this luxury. In a few cases they could do experiments but for most situations, they had to resort theoretical predictions. Most approaches used to predict stability of fluid flows fall under the category of **Small Disturbance Theory** [18].

In any typical small disturbance analysis, the basic flow variable is considered to be under small perturbations. As a result of including perturbations into the governing equations of the particular fluid flow, the so-called disturbance/perturbation equations are obtained. However, in order to calculate the eigen-values that define the stability of the considered flow, it is necessary to linearize and then solve the disturbance equations.

In the following pages, a small disturbance analysis is applied to predict the free-shear flow instability, that is, the Kelvin-Helmholtz instability. To do so, two flows of different velocities and densities separated by a horizontal surface are considered (Figure 2.9)

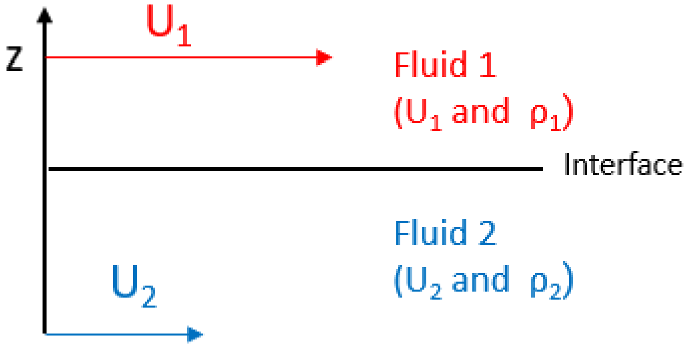

Figure 2.9: Kelvin-Helmholtz Stability problem [18].

Moreover, both flows are considered to be potential, that is, irrotational, incompressible and inviscid. As a result, the Laplace equation is satisfied as well as the unsteady Bernoulli´s equation [18]:

$$p_i = C_i - \rho_i \frac{\partial \phi_i}{\partial t} - \frac{\rho_i}{2} \mid \nabla \phi_i \mid^2 - \rho_i g z \quad for \ i = 1, 2 \tag{2.7}$$

For the base undisturbed flow this equation can be simplified:

$$C_1 - \frac{\rho_1}{2} U_1^2 = C_2 - \frac{\rho_2}{2} U_2^2 \tag{2.8}$$

For such flows, the velocity potential and the hydrostatic pressure distribution is given by the following equations:

$$\begin{cases} \phi_1 = U_1 x \ p_1 = P_0 - \rho_1 g z & \text{for } z < 0 \\ \phi_2 = U_2 x \ p_2 = P_0 - \rho_2 g z & \text{for } z > 0 \end{cases} \tag{2.9}$$

Following the previous stated procedure for the small disturbance analysis, a perturbation is then applied for both the velocity potential equations:

$$\phi_1 = U_1 x + \hat{\phi_1}\,(x, y, z)\, \phi_2 = U_2 x \hat{\phi_2}\,(x, y, z) \tag{2.10}$$

Moreover, applying the far-field boundary condition, disturbances are considered to be finite only at the interface and thereby, their value can be neglected far away from the interface.

Two types of interface boundary conditions can be satisfied by the system, these are: the Kinematic and Dynamic boundary conditions.

The kinematic condition at the interface requires that the vertical velocity of the two fluids match. Mathematically, this can be written as:

$$\omega_i = \frac{\partial \phi_i}{\partial z} = \frac{d\zeta}{dt} = \frac{\partial \zeta}{\partial t} + \frac{\phi_i}{\partial x}\frac{\zeta}{\partial x} \tag{2.11}$$

On the other hand, the dynamic condition at the interface requires that the pressure is constant across the interface. Based on this, the following relations can be written for the interface between the two fluids before and after imposing the disturbance.

$$C_1 - \frac{\rho_1}{2}U_1^2 = C_2 - \frac{\rho_2}{2}U_2^2 \quad for\ z = 0 \tag{2.12}$$

$$p_i = C_i - \rho_i \frac{\partial \phi_i}{\partial t} - \frac{\rho_i}{2} \mid \nabla \phi_i \mid^2 - \rho_i g z \quad for\ i = 1, 2 \quad and z \lesseqgtr 0 \tag{2.13}$$

If perturbations are considered to be weak, only causing very small displacements of the interface, and also ignoring the higher ordered terms, the relations obtained from both the kinematic and dynamic conditions can be recasted as:

$$\frac{\partial \hat{\phi}_1}{\partial x} \approx \frac{\partial \zeta}{\partial t} + U_1 \frac{\partial \zeta}{\partial x} \tag{2.14}$$

$$\frac{\partial \hat{\phi}_2}{\partial x} \approx \frac{\partial \zeta}{\partial t} + U_2 \frac{\partial \zeta}{\partial x} \tag{2.15}$$

$$\rho_1 \left(U_1 \frac{\partial \hat{\phi}_1}{\partial x} + \frac{\partial \hat{\phi}_1}{\partial t} + g\zeta \right) \approx \rho_2 \left(U_2 \frac{\partial \hat{\phi}_2}{\partial x} + \frac{\partial \hat{\phi}_2}{\partial t} + g\zeta \right) \tag{2.16}$$

Up to this point, a new assumption is considered. This new assumption consists on considering simple two dimensional disturbances, that is:

$$\zeta = \zeta_0 e^{i(\alpha x - \omega t)} \tag{2.17}$$

$$\hat{\phi}_j = \phi_j'(z) e^{i(\alpha x - \omega t)} \tag{2.18}$$

Where α is a real number that represents the wave number and ω is a complex number that represents the frequency of the perturbation.The disturbance will be amplified and make the fluid interface unstable if the imaginary part of omega is positive.

Substituting this perturbation into the Laplace equation and employing the far-field boundary condition,the amplitudes of the perturbation will be obtained:

$$\phi_2' = A_1 e^{kz}, \quad \phi_2' = A_2 e^{kz}, \tag{2.19}$$

Using these amplitudes and the interface kinematic condition, the values of the unknown quantities can be extracted:

$$A_1 = i\zeta_0 \left(U_1 - \frac{\omega}{\alpha}\right) \quad A_2 = -i\zeta_0 \left(U_2 - \frac{\omega}{\alpha}\right) \tag{2.20}$$

Substituting the perturbation into the dynamic condition and extracting the roots of the subsequent quadratic equation, the desired eigen-values are obtained.

$$\omega = \alpha \frac{\rho_1 U_1 + \rho_2 U_2}{\rho_1 + \rho_2} \pm \sqrt{\left[\frac{\alpha^2 \rho_1 \rho_2 \left(U_1 - U_2\right)^2}{\left(\rho_1 + \rho_2\right)^2} - \frac{\alpha g \left(\rho_1 - \rho_2\right)}{\rho_1 + \rho_2}\right]} \tag{2.21}$$

The stability of the fluid is dependent on the value of the squared term. The disturbance is unstable if the value is negative, neutral if the value is 0 and stable if the value is positive. Therefore, the unstable condition is given by the following relation:

$$\left(U_1 - U_2\right)^2 > \frac{g\left(\rho_1^2 - \rho_2^2\right)}{\alpha \rho_1 \rho_2} \tag{2.22}$$

Until now, the prediction of instability has been discussed for free-shear flows. A similar methodology can be applied to characterize the stability for parallel viscous flows, which describes the flow inside laminar boundary layers.

The perturbation form of the 2D incompressible Navier Stockes equations are :

$$\frac{\partial u\prime}{\partial x} + \frac{\partial \nu\prime}{\partial y} = 0 \tag{2.23}$$

$$\frac{\partial u'}{\partial t} + U\frac{\partial u'}{\partial x} + \nu'\frac{\partial U}{\partial y} + \frac{1}{\rho}\frac{\partial \rho'}{\partial x} = \nu \nabla u' \tag{2.24}$$

$$\frac{\partial \nu'}{\partial t} + U\frac{\partial \nu'}{\partial x} + \frac{1}{\rho}\frac{\partial \rho'}{\partial y} = \nu \nabla \nu' \tag{2.25}$$

Assuming a disturbance in the form of a wave travelling in the axial direction, the stream function of a single mode in the perturbation can be written in the following form:

$$\psi\left(x, y, t\right) = \psi(y)e^{t(\alpha x - \omega t)} \tag{2.26}$$

Where ω is a complex number whose real part (ω_r) represents the frequency of the mode, and the imaginary part (ω_i)is the amplification factor. If ($\omega_i < 0$) the wave is damped and therefore the flow is stable. However, if ($\omega_i > 0$), instabilities are present in the system.

From the stream function, the velocity components can be derived. These are:

$$u' = \frac{\partial \psi}{\partial y} = \psi'(y)e^{i(\alpha x - \omega t)} \quad \nu' = -\frac{\partial \psi}{\partial x} = -i\alpha\psi(y)e^{i(\alpha x - \omega t)} \tag{2.27}$$

Substituting these velocity components into the disturbance equations and rearranging the equation so that the pressure term is eliminated, a 4th order differential equation for the amplitude function is obtained:

$$(U - c)\left(\psi'' - \alpha^2\psi\right) - U''\psi = -\frac{1}{\alpha Re}\left(\psi'''' - 2\alpha^2\psi'' + \alpha^4\psi\right) \tag{2.28}$$

This approach, known as the Orr-Sommerfeld equation, describes the hydrodynamic stability characteristic of viscous parallel flows. Moreover, it represents an eigenvalue problem with the following boundary conditions:

$$y = 0 \ : u' = \nu' = 0 \quad y = \infty \ : u' = \nu' = 0 \tag{2.29}$$

The results obtained after solving the equation can be visualized in the form of curves, known as the neutral stability curves or thumb curves. In this curves the region inside the thumb represents the conditions where the disturbances are amplified, thus, transition begins [18].

In the case of the Reynolds number thumb curve (Figure 2.10), parameter with high influence over transition, the lower limit at which the disturbances start amplifying, thus, transition starts, is called the *Critical Reynolds Number*.

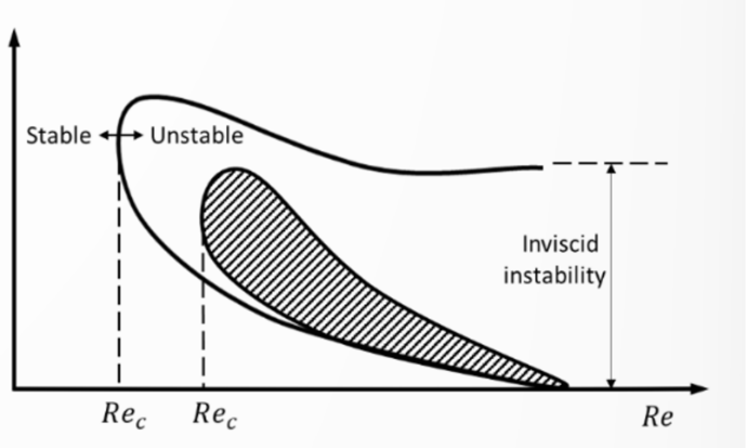

Figure 2.10: Neutral Curves for Orr-Sommerfeld equation [18].

The value of the critical Reynolds number can vary depending on the flow conditions being considered. In the case of flow over a flat plate, case employed in the project to validate results, is usually in the range of $10^5 < Re_cx < 3 * 10^6$ depending on the turbulence intensity of the freestream as well as on the surface roughness. However, a value of $5 * 10^5$ is a well-used approximation [14].

2.2.1 Effect of Heat Transfer

As it has been previously mentioned, the onset to transition depends on multiple factors. One of them can be the effect of heat transfer, which will be computed in the project.

In gases, when temperature increases, so does viscosity. Due to this, when the wall becomes warmer than the surrounding fluid, that is, when a negative temperature gradient is developed in the wall, also a negative viscosity gradient rises. As a result,an unstable boundary layer is reached. If instead, the temperature is decreased, the boundary layer will become more stable. However, when working with liquids, the behaviour is the other way around. For liquids, viscosity decreases when temperature increases, thus, heating processes ends up in more stable boundary layers and the cooling processes in more unstable boundary layers [17].

Based on that,when cooling occurs, that is, when heat transfer goes from the boundary layer to the wall, the boundary layer stabilises, and thereby, transition is delayed. However, when heating takes place instead, the boundary layer destabilizes. As a result, a reduction on the critical Reynolds number is obtained [17].

2.3 Heat Transfer Resistance Modelling

Up to this point, and in order to be able to analyze the behaviour of the flow in the geometry considered in this project, it is necessary to employ the so-called thermal resistance method.

The thermal resistance method compares heat transfer processes with electrical circuits (Equation 2.30). To do so, it establishes that the temperature can be seen as the voltage (V) and the heat flux as the current intensity (I).

$$\frac{V_{s1} - V_{s2}}{I} = R_e \longrightarrow \frac{T_{s1} - T_{s2}}{q_x} = R_t \tag{2.30}$$

Moreover, in the case of resistance, it establishes that the value will vary depending on the heat transfer methods that are being considered. Thereby, different thermal resistances can be defined:

Thermal resistance for conduction

$$R_{t,cond} = \frac{L}{kA} \tag{2.31}$$

Thermal resistance for convection

$$R_{t,conv} = \frac{1}{hA} \tag{2.32}$$

Thermal resistance for radiation

$$R_{t,rad} = \frac{1}{h_r A} \tag{2.33}$$

In the case of having a process like the one shown in Figure 2.11, in which there is a hot fluid at a temperature $T_{\infty 1}$ and a cold fluid at a temperature $T_{\infty 2}$, both flowing on the opposite sides of a wall with a thermal conductivity k, the wall surface will present two different temperatures: the hot surface temperature (T_{s1}) and the cold surface temperature (T_{s1}). As a result of this temperature difference, a heat flux will appear and thereby, a change in the temperature along the system.

If the previously explained analogy is now applied, and taking into consideration that the heat flux through the whole network is constant, the thermal resistance for the different subsystems can be grouped, thus, a unique and whole equation is obtained for the problem.

$$q_x = \frac{T_{\infty 1} - T_{\infty 2}}{R_{total}} \tag{2.34}$$

$$R_{total} = \frac{1}{h_1 A} + \frac{L}{kA} + \frac{1}{h_2 A} \tag{2.35}$$

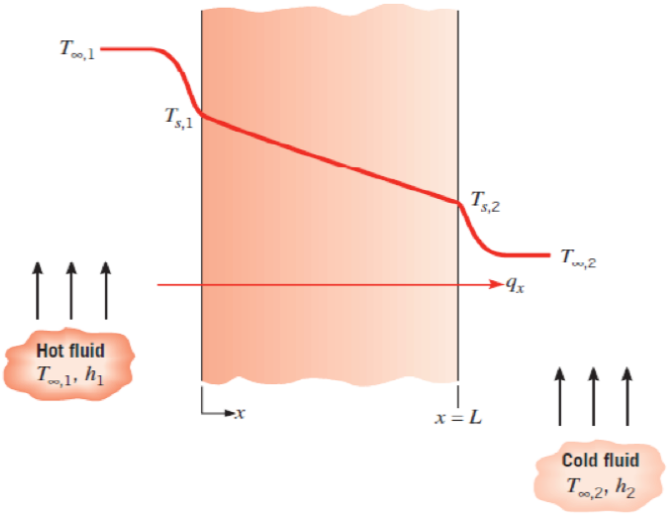

Figure 2.11: Heat transfer through the wall [14].

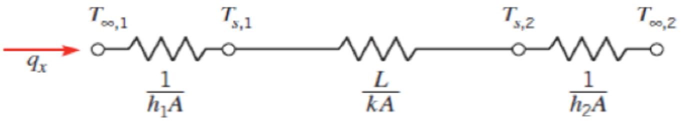

Figure 2.12: Resistance equivalent [14].

2.4 Governing Equations

In **ANSYS CFX** [19], the main equations that model the mass and heat transfer throughout the entire system will be solved by an iteration process.

The instantaneous equations of mass, momentum and energy conservation can be written as follows when defined in a stationary frame [20]:

The continuity equation

$$\frac{\partial \rho}{\partial t} + \nabla \cdot (\rho \mathbf{U}) = 0 \tag{2.36}$$

The momentum equation

$$\frac{\partial (\rho \mathbf{U})}{\partial t} + \nabla \cdot (\rho \mathbf{U} \otimes \mathbf{U}) = -\nabla p + \nabla \cdot \tau + \mathbf{S}_M \tag{2.37}$$

The parameter τ is known as the stress tensor and its value is related to the strain rate by the following expression:

$$\tau = \mu \left(\nabla \mathbf{U} + (\nabla U)^T - \frac{2}{3} \delta \, \nabla \cdot \mathbf{U} \right) \tag{2.38}$$

The total energy equation

$$\frac{\partial (\rho h_{tot})}{\partial t} - \frac{\partial \rho}{\partial t} + \nabla \cdot (\rho \mathbf{U} h_{tot}) = \nabla \cdot (\lambda \nabla T) + \nabla \cdot (\mathbf{U} \cdot \tau) + \mathbf{U} \cdot \mathbf{S}_M + \mathbf{S}_E \tag{2.39}$$

Where:

- h_{tot} is the total entalphy whose value is related with the static entalphy h (T,p) by the following expression:

$$h_{tot} = h + \frac{1}{2} \mathbf{U}^2 \tag{2.40}$$

- $\nabla \cdot (\mathbf{U} \cdot \tau)$ is the viscous work term, whose value represents the work done by viscous stresses.

- $\mathbf{U} \cdot \mathbf{S}_M$, although its value is neglected, this term represents the work done by external momentum sources.

2.5 CFD Modeling

2.5.1 Reynolds Averaged Navier Stockes Equations (RANS)

As explained before, the previous governing equations are suitable for stationary-state processes. However, turbulent flows, which originate when the viscous forces become negligible compared to inertia forces, thus, when the flow is defined by high Reynolds Numbers, are characterized due to their their three-dimensional component, their unsteady and its multiple scales. This properties, which are a direct consequence of the fluctuations, in both space and time, which characterize a turbulent flow, leads to the need of averaging the previous defined equations by using turbulence models. The use of turbulence models will avoid the appearance of computational problems mainly caused because of the shorter length scales turbulent flows require in comparison with the smallest finite volume mesh.

The new models are developed taking into account what happens when big timescales are considered. In such processes,two different components can be distinguished, the average and the fluctuating component. Taking this into account, the Navier-Stokes equations can be modified leading to the Reynolds Averaged Navier-Stockes (RANS) equations, which will enable the process to have less computational effort [21].

Based on that, the averaged governing equations are:

The continuity equation

$$\frac{\partial \rho}{\partial t} + \frac{\partial}{\partial x_j}\left(\rho U_j\right) = 0 \tag{2.41}$$

The momentum equation

$$\frac{\partial\left(\rho U_i\right)}{\partial t} + \frac{\partial}{\partial x_i}\left(\rho U_i U_j\right) = -\frac{\partial p}{\partial x_i} + \frac{\partial}{\partial x_j}\left(\tau_{ij} - \rho\overline{u_i u_j}\right) + \mathbf{S}_m \tag{2.42}$$

The total energy equation

$$\frac{\partial\left(\rho h_{tot}\right)}{\partial t} - \frac{\partial \rho}{\partial t} + \frac{\partial}{\partial x_j}\left(\rho U_j h_{tot}\right) = \frac{\partial}{\partial x_j}\left(\lambda\frac{\partial T}{\partial x_j} - \rho\overline{u_j h}\right) + \frac{\partial}{\partial x_j}\left[U_i\left(\tau_{ij} - \rho\overline{u_i u_j}\right)\right] + \mathbf{S}_E \tag{2.43}$$

$$h_{tot} = h + \frac{1}{2}U_i U_j + k \tag{2.44}$$

$$U_i k = \frac{1}{2}\overline{u_i^2} \tag{2.45}$$

2.5.2 Eddy Viscosity Turbulence Models

These group of models propose turbulence to be small eddies which are continuously dissipating and forming. In addition, these models consider the Reynolds stresses to be proportional to the mean velocity gradients as well as to the eddy (turbulent) viscosity by the gradient diffusion hypothesis as [22]:

$$-\rho\overline{u_i u_j} = \mu_t\left(\frac{\partial U_i}{\partial x_j}+\frac{\partial U_j}{\partial x_i}\right)-\frac{2}{3}\delta_{ij}\left(\rho k+\mu_t\frac{\partial U_k}{\partial x_k}\right) \tag{2.46}$$

Where μ_t, which should be known, is the eddy viscosity or turbulent viscosity.

Similar to the eddy viscosity hypothesis, the eddy diffusivity hypothesis states that the Reynolds fluxes of a scalar are linearly related to the mean scalar gradient [22]:

$$-\rho\overline{u_i\varphi} = \Gamma_t\frac{\partial \Phi}{\partial x_i} \tag{2.47}$$

Where Φ_t is the eddy diffusivity:

$$\Phi = \frac{\mu_t}{Pr_t} \tag{2.48}$$

Where Pr_t is the turbulent Prandtl number.

Based on the previous hypothesis, the Reynolds averaged momentum and scalar transport equations are [22]:

$$\frac{\partial \rho U_i}{\partial t}+\frac{\partial}{\partial x_j}\left(\rho U_i U_j\right) = -\frac{\partial p\prime}{\partial x_i}+\frac{\partial}{\partial x_j}\left[\mu_{eff}\left(\frac{\partial U_i}{\partial x_j}+\frac{\partial U_j}{\partial x_i}\right)\right]+S_M \tag{2.49}$$

Where S_M is the body force´s sum, $p\prime$, is the modified pressure, and μ_{eff} is the Effective Viscosity [22]:

$$p\prime = p+\frac{2}{3}\rho k+\frac{2}{3}\mu_{eff}\frac{\partial U_k}{\partial x_k} \tag{2.50}$$

$$\mu_{eff} = \mu+\mu_t \tag{2.51}$$

The Reynolds averaged energy equation becomes:

$$\frac{\partial \rho h_{tot}}{\partial t} - \frac{\partial \rho}{\partial t} + \frac{\partial}{\partial x_j}\left(\rho U_j h_{tot}\right) = \frac{\partial}{\partial x_j}\left(\lambda \frac{\partial T}{\partial x_j} + \frac{\mu_t}{Pr_t}\frac{\partial h}{\partial x_j}\right) + \frac{\partial}{\partial x_j}\left[U_i\left(\tau_{ij} - \rho\overline{u_i u_j}\right)\right] + S_E \tag{2.52}$$

The Reynolds averaged transport equation for additional variables, that is, non-reacting scalars, becomes:

$$\frac{\partial \rho \Phi}{\partial t} + \frac{\partial}{\partial x_j}\left(\rho U_j \Phi\right) = \frac{\partial}{\partial x_j}\left[\left(\Gamma_\Phi + \frac{\mu_t}{\sigma_\Phi}\right)\frac{\partial \Phi}{\partial x_j}\right] + S_\Phi \tag{2.53}$$

2.5.3 Two Equation Turbulence Models

The two-equation turbulence models are commonly used as they propose a great compromise between computational accuracy and numerical effort [22].

In this kind of models, both the length scale and the velocity are solved by using different transport equations. Furthermore, in these models the gradient diffusion hypothesis is employed to relate the Reynolds stresses to the mean velocity gradients as well as to the turbulent viscosity, which is modeled as the product of a turbulent velocity and turbulent length scale. However, in order to estimate the turbulence velocity scale, these models employ the turbulent kinetic energy whose value is derived from its transport equation. On the other hand, the turbulent length scale is determined by the use of two different properties of the turbulence field, generally the turbulent kinetic energy and its dissipation rate, which is obtained from its transport equation [22].

2.5.3.1 The K-Epsilon Model

The K-ϵ model predicts reasonable accurate results for attached flows away from the wall. In the model, k, known as the turbulence kinetic energy and expressed in m^2/s^2, is described as the variance of the fluctuations in velocity and ϵ, known as the turbulence eddy dissipation and expressed in m^2/s^3, is defined as the rate at which the velocity fluctuations dissipate.

In addition, the k-ϵ model is also based on the eddy viscosity. Thus, relations stated in section 2.5.2 are employed. However, this model assumes that the turbulence viscosity is linked to the turbulence kinetic energy and dissipation by:

$$\mu_t = C_\mu \rho \frac{k^2}{\epsilon} \tag{2.54}$$

Where C_μ is a constant whose value is 0.09.

The values of **k** and ϵ are obtained directly from the differential transport equations for the turbulence kinetic energy and turbulence dissipation rate:

$$\frac{\partial(\rho k)}{\partial t}+\frac{\partial}{\partial x_j}(\rho U_j k)=\frac{\partial}{\partial x_j}\left[\left(\mu+\frac{\mu_t}{\sigma_k}\right)\frac{\partial k}{\partial x_j}\right]+P_k-\rho\epsilon+P_{kb} \tag{2.55}$$

$$\frac{\partial(\rho \epsilon)}{\partial t}+\frac{\partial}{\partial x_j}(\rho U_j \epsilon)=\frac{\partial}{\partial x_j}\left[\left(\mu+\frac{\mu_t}{\sigma_k}\right)\frac{\partial \epsilon}{\partial x_j}\right]+\frac{\epsilon}{k}\left(C_{\epsilon 1}P_k-C_{\epsilon 2}\rho\epsilon+C_{\epsilon 1}P_{\epsilon b}\right) \tag{2.56}$$

Where $C_{\epsilon 1}=1.44$, $C_{\epsilon 2}=1.92$, $\sigma_k=1$ and $\sigma_\epsilon=1.3$ are constants. P_{kb} and $P_{\epsilon b}$ represent the buoyancy forces´s influence and P_k is the turbulence production due to viscous forces whose value is modeled by:

$$P_k=\mu_t\left(\frac{\partial U_i}{\partial x_j}+\frac{\partial U_j}{\partial x_i}\right)\frac{\partial U_i}{\partial x_j}-\frac{2}{3}\frac{\partial U_k}{\partial x_k}\left(3\mu_t\frac{\partial U_k}{\partial x_k}+\rho k\right) \tag{2.57}$$

$$P_{\epsilon b}=C_3\cdot max\left(0,P_{kb}\right) \tag{2.58}$$

If the buoyancy model is employed:

$$P_{kb}=-\frac{\mu_t}{\rho\sigma_\rho}g_i\frac{\partial\rho}{\partial x_i} \tag{2.59}$$

If the Boussinesq buoyancy model is used:

$$P_{kb}=\frac{\mu_t}{\rho\sigma_\rho}\rho\beta g_i\frac{\partial T}{\partial x_i} \tag{2.60}$$

With default constant values of turbulence Schmidt number (σ_ρ) of 0.9 for Boussinesq buoyancy and 1 for buoyancy model and dissipation coefficient (C_3) of 1.

2.5.3.2 The K-Omega Model

The k-ω model enables the near-wall treatment for low-Reynolds number computations. Moreover, in comparison with the k-ϵ model, which requires high-resolution mesh near the wall (y^+<0.2), the k-ω allows using more achievable values ($y^+ < 2$), what makes it a robust and accurate model [22]. In addition, the k-ω model considers the turbulence viscosity to be related with the turbulence kinetic energy and turbulence frequency by:

$$\mu_t=\rho\frac{k}{\omega} \tag{2.61}$$

This model, developed by Wilcox [22], establishes that the k (turbulent kinetic energy) and ω (turbulence frequency) can be obtained by:

$$\frac{\partial\left(\rho k\right)}{\partial t}+\frac{\partial}{\partial x_j}\left(\rho U_j k\right)=\frac{\partial}{\partial x_j}\left[\left(\mu+\frac{\mu_t}{\sigma_k}\right)\frac{\partial k}{\partial x_j}\right]+P_k-\beta\prime\rho k\omega+P_{kb} \tag{2.62}$$

$$\frac{\partial\left(\rho\omega\right)}{\partial t}+\frac{\partial}{\partial x_j}\left(\rho U_j\omega\right)=\frac{\partial}{\partial x_j}\left[\left(\mu+\frac{\mu_t}{\sigma_\omega}\right)\frac{\partial\omega}{\partial x_j}\right]+\alpha\frac{\omega}{k}P_k-\beta\rho\omega^2+P_{\omega b} \tag{2.63}$$

$$-\rho\overline{u_i u_j}=\mu_t\left(\frac{\partial U_i}{\partial x_j}+\frac{\partial U_j}{\partial x_i}\right)-\frac{2}{3}\delta_{ij}\left(\rho k+\mu_t\frac{\partial U_k}{\partial x_k}\right) \tag{2.64}$$

Where P_k is obtained from equation 2.57, buoyancy terms are the previously explained ones (Equations 2.59 and 2.60), with $\beta\prime = 0.09$, $\alpha = \frac{5}{9}$, $\beta = 0.075$, $\sigma_k = 2$, $\sigma_\omega = 2$ and $P_{\omega b}$ obtained as:

$$P_{\omega b}=\frac{\omega}{k}\left(\left(\alpha+1\right)C_3 max\left(P_{kb},0\right)-P_{kb}\right) \tag{2.65}$$

2.5.3.3 The Shear Stress Transport (SST) Model

In order to minimize problems such as the high dependence on the specified ω at the inlet or the strong sensitivity to freestream conditions, a combination of the k-ϵ model in outer regions and the k-ω model near the surface is employed. This method provides highly accurate predictions of the onset and the amount of flow separation under adverse pressure gradients as it establishes a limiter to the eddy-viscosity formulation:

$$\nu_t = \frac{a_1 k}{max\left(a_1, \omega, SF_2\right)} \tag{2.66}$$

$$\nu_t = \frac{\mu_t}{\rho} \tag{2.67}$$

Where S is an invariant measure of the strain rate, F_2 a blending function which restricts the limiter to the wall boundary layer, and $\sigma_{k1} = 1.176$

2.5.3.3.1 Blending Functions

The blending functions are of big importance for the success of the method. They are based on the flow variables as well as on the distance to the nearest surface.

$$F_1 = tanh\left(arg_1^4\right) \tag{2.68}$$

$$arg_1 = min\left(max\left(\frac{\sqrt{k}}{\beta'\omega y'}, \frac{500\nu}{y^2\omega}\right), \frac{4\rho k}{CD_{k\omega}\sigma_{\omega 2} y^2}\right) \tag{2.69}$$

$$CD_{k\omega} = max\left(2\rho\frac{1}{\sigma_{\omega 2}\omega}\frac{\partial k}{\partial x_j}\frac{\partial \omega}{\partial x_j}, 1.0 \times 10^{-10}\right) \tag{2.70}$$

$$F_2 = tanh\left(arg_2^2\right) \tag{2.71}$$

$$arg_2 = max\left(\frac{2\sqrt{k}}{\beta'\omega y'}, \frac{500\nu}{y^2\omega}\right) \tag{2.72}$$

In where ν is the kinematic viscosity and y is the distance to the nearest wall.

2.5.4 Laminar-Turbulent Transition Models

As mentioned in subsection 2.1.3.1, in the fluid flow three regions can be distinguished. In order to model both the laminar and transition region, two different transition models can be employed. These are: the Two Equation Gamma Theta Transition Model and the One Equation Intermittency Model.

During the following pages, both transition models are going to be explained.

2.5.4.1 Two Equation Gamma Theta Transition Model

The Two Equation Gamma Theta Transition Model turns out to be the most suitable one for general purposes. Moreover,it employs two different transport equations, one for the intermittency and another one for the transition onset criteria in terms of momentum thickness Reynolds number.

The **transport equation for the intermittency** (γ):

$$\frac{\partial\left(\rho\gamma\right)}{\partial t}+\frac{\partial\left(\rho U_j\gamma\right)}{\partial x_j}=P_{\gamma 1}-E_{\gamma 1}+P_{\gamma 2}-E_{\gamma 2}+\frac{\partial}{\partial x_j}\left[\left(\mu+\frac{\mu_t}{\sigma_\gamma}\right)\frac{\partial\gamma}{\partial x_j}\right] \tag{2.73}$$

$$P_{\gamma 1}=2F_{lenght}\rho S\left[\gamma F_{onset}\right] \tag{2.74}$$

$$E_{\gamma 1}=P_{\gamma 1}\gamma \tag{2.75}$$

$$P_{\gamma 2}=\left(2c_{\gamma 1}\right)\rho\Omega\gamma F_{turb} \tag{2.76}$$

$$E_{\gamma 2}=c_{\gamma 2}P_{\gamma 2}\gamma \tag{2.77}$$

Where $c_{\gamma 1}=0.03$, $c_{\gamma 2}=50$, $c_{\gamma 3}=0.5$ and $\alpha_\gamma=1.0$ are the intermittency constants and S, the parameter that represents the strain value. On the other hand, the parameter ω is the magnitude of vorticity rate and F_{length} is an empirical correlation which controls the length of the transition region.

The transition onset in modeled by:

$$Re_\nu=\frac{\rho y^2 S}{\mu} \tag{2.78}$$

$$Re_T = \frac{\rho k}{\mu \omega} \tag{2.79}$$

$$F_{onset1} = \frac{Re_\nu}{2.193 Re_{\theta c}} \tag{2.80}$$

$$F_{onset2} = min\left(max\left(F_{onset1}, F_{onset1}^4\right), 2.0\right) \tag{2.81}$$

$$F_{onset3} = max\left(1 - \left(\frac{R_T}{2.5}\right)^3, 0\right) \tag{2.82}$$

$$F_{onset} = max\left(F_{onset2} - F_{onset3}, 0\right) \tag{2.83}$$

$$F_{turb} = e^{-\left(\frac{R_T}{4}\right)^4} \tag{2.84}$$

The parameter $Re_{\theta c}$ is the Critical Reynolds number and represents the value in which the intermittency first starts to increase in the boundary layer.

The transport equation for the transition momentum thickness Reynolds number ($\widetilde{Re_{\theta t}}$) is:

$$\frac{\partial\left(\rho \widetilde{Re_{\theta t}}\right)}{\partial t} + \frac{\partial\left(\rho U_j \widetilde{Re_{\theta t}}\right)}{\partial x_j} = P_{\theta t} + \frac{\partial}{\partial x_j}\left[\sigma_{\theta t}\left((\mu + \mu_t)\frac{\partial \widetilde{Re_{\theta t}}}{\partial x_j}\right)\right] \tag{2.85}$$

$$P_{\theta t} = c_{\theta t}\frac{\rho}{t}\left(Re_{\theta t} - \widetilde{Re_{\theta t}}\right)(1.0 - F_{\theta t}) \tag{2.86}$$

$$t = \frac{500\mu}{\rho U^2} \tag{2.87}$$

$$F_{\theta t} = min\left(max\left(F_{wake} e^{-\left(\frac{y}{\delta}\right)^4}, 1.0 - \left(\frac{\gamma - \frac{1}{50}}{1.0 - \frac{1}{50}}\right)^2\right), 1.0\right) \tag{2.88}$$

$$\theta_{BL} = \frac{\mu \widetilde{Re_{\theta t}}}{\rho U} \tag{2.89}$$

$$\delta_{BL} = \frac{15}{2}\theta_{BL} \tag{2.90}$$

$$\delta = \frac{50\Omega y}{U}\delta_{BL} \tag{2.91}$$

$$Re_{\omega} = \frac{\rho\omega y^2}{\mu} \tag{2.92}$$

$$F_{wake} = e^{\left(\frac{Re_{\omega}}{10^5}\right)^2} \tag{2.93}$$

Where $c_{\theta t} = 0.03$ and $\sigma_{\theta t} = 2.0$. The parameter $Re_{\theta t}$ is the transition onset and its value can be determined as follows:

$$Re_{\theta t} = \begin{cases} \left[1173.51 - 589.428Tu + \frac{0.2196}{Tu^2}\right] F(\lambda_\theta) & \text{for } Tu \leq 1.3 \\ 331.50\,[Tu - 0.5658]^{-0.671}\,F(\lambda_\theta) & \text{for } Tu > 1.3 \end{cases} \tag{2.94}$$

$$F(\lambda_\theta) = \begin{cases} 1 - [-12.986\lambda_\theta - 123.66\lambda_{\theta^2} - 405.689\lambda_{\theta^3}]\,e^{-\left[\frac{Tu}{1.5}\right]^{1.5}} & \text{for } \lambda_\theta \leq 0 \\ 1 + 0.275\left[1 - e^{-35.0\lambda_\theta}\right] e^{\frac{-Tu}{0.5}} & \text{for } \lambda_\theta > 0 \end{cases} \tag{2.95}$$

$$\lambda_\theta = \left(\frac{\theta^2}{\nu}\right)\frac{dU}{ds} \tag{2.96}$$

Where Tu is the local turbulence intensity, λ_θ the Thwaites pressure gradient coefficient and $\frac{dU}{ds}$ is the acceleration in the streamwise direction.

To calculate the length of the transition region, that is F_{length}, is necessary to include a modification in order to avoid a sharp increase in the boundary layer´s skin friction in the boundary layer after the transition:

$$F_length = \begin{cases} \left[398.189E - 1 + (-119.270E - 4)\,\tilde{Re_{\theta t}} + (-132.567E - 6)\,\tilde{Re_{\theta t}}^2\right], \tilde{Re_{\theta t}} < 400 \\ \left[263.404 + (-123.939E - 2)\,\tilde{Re_{\theta t}} + (194.548E - 5)\,\tilde{Re_{\theta t}}^2 + (-101.695E - 8)\,\tilde{Re_{\theta t}}^3\right], 400 \leq \tilde{Re_{\theta t}} < 596 \\ \left[0.5 - \left(\tilde{Re_{\theta t}} - 596.0\right) \cdot 3.0E - 4\right], 596 \leq \tilde{Re_{\theta t}} < 1200 \\ [0.3188]\,, 1200 \leq \tilde{Re_{\theta t}} \end{cases} \tag{2.97}$$

$$F_{sublayer} = e^{-\left(\frac{R_\omega}{0.4}\right)^2} \tag{2.98}$$

$$R_\omega = \frac{\rho y^2 \omega}{500\mu} \tag{2.99}$$

$$F_{length} = F_{length} * (1 - F_{sublayer}) + 40.0 F_{sublayer} \tag{2.100}$$

The parameter $Re_{\theta c}$ is the value for which the turbulence starts to develop, where as $Re_{\theta t}$ is the point in which the velocity starts to present a turbulence behaviour. In addition, the parameter $Re_{\theta c}$ is the point in which the model is defined in order to match F_{length} and $Re_{\theta t}$. The value of $Re_{\theta c}$ can be estimated by the following expression:

$$R_{\theta c} = \begin{cases} \left[\tilde{Re_{\theta t}} - \begin{pmatrix} 396.03510^{-2} + \left(-120.65610^{-4}\right) \tilde{Re_{\theta t}} & + \left(868.23010^{-6}\right) \tilde{Re_{\theta t}}^{2} \\ + \left(-696.50610^{-9}\right) \tilde{Re_{\theta t}}^{3} & + \left(174.10510^{-12}\right) \tilde{Re_{\theta t}}^{4} \end{pmatrix}\right] & \text{for } \tilde{Re_{\theta t}} \leq 1870 \\ \left[\tilde{Re_{\theta t}} - \left(593.11 + \left(\tilde{Re_{\theta t}} - 1870.0\right) \cdot 0.482\right)\right], & \text{for } \tilde{Re_{\theta t}} > 1870 \end{cases} \tag{2.101}$$

Coupling the transition model with the STT model, it is obtained that:

$$\frac{\partial}{\partial t}(\rho k) + \frac{\partial}{\partial x_j}(\rho u_j k) = \tilde{P_k} - \tilde{D_k} + \frac{\partial}{\partial x_j}\left((\mu + \sigma_k \mu_t)\frac{\partial k}{\partial x_j}\right) \tag{2.102}$$

In where:

$$\tilde{P_k} = \gamma_{eff} P_k \tag{2.103}$$

$$\tilde{D_k} = min\left(max\left(\gamma_{eff}, 0.1\right), 1.0\right) D_k \tag{2.104}$$

$$R_y = \frac{\rho y \sqrt{k}}{\mu} \tag{2.105}$$

$$F_3 = e^{-\left(\frac{R_y}{120}\right)^8} \tag{2.106}$$

$$F_1 = max\left(F_{1orig}, F_3\right) \tag{2.107}$$

In which the values of P_k, F_{1orig} and D_k are obtained from the initial SST model.

2.5.4.2 One Equation Intermittency Transition Model

The Intermittency transition model employs only one transport equation to solve the turbulence intermittency (γ). In comparison with the previous seen model (Subsection 2.5.4.1), the intermittency model reduces the computational effort as well as it allows it´s use on surfaces with relative motion around the coordinate system due to it dodges the dependency of the Re_θ equation on the speed (U). In addition, this transition model can only be employed in wall-bounded flows analysis [22].

The **transport equation for intermittency** is:

$$\frac{\partial(\rho\gamma)}{\partial t} + \frac{\partial(\rho U_j \gamma)}{\partial x_j} = P_\gamma - E_\gamma + \frac{\partial}{\partial x_j}\left[\left(\mu + \frac{\mu_t}{\sigma_\gamma}\right)\frac{\partial \gamma}{\partial x_j}\right] \tag{2.108}$$

In where:

$$P_\gamma = F_{length}\rho S\gamma\left(1-\gamma\right)F_{onset} \tag{2.109}$$

$$E_\gamma = C_{a2}\rho\Omega\gamma F_{turb}\left(C_{e2}\gamma - 1\right) \tag{2.110}$$

In which $F_{length} = 100$ and **S** is the so-called strain rate. Moreover, E_γ is the destruction/relaminarization source in which, Ω is the absolute vorticity rate and $c_{a2} = 0.06$, $c_{e2} = 50$ and $\Omega\gamma = 1$ [22].

The transition onset is modeled by:

$$F_{onset1} = \frac{Re_\nu}{2.2Re_{\theta c}} \tag{2.111}$$

$$F_{onset2} = min\left(F_{onset1}, 2.0\right) \tag{2.112}$$

$$F_{onset3} = max\left(1 - \left(\frac{R_T}{3.5}\right)^3, 0\right) \tag{2.113}$$

$$F_{onset} = max\left(F_{onset2} - F_{onset3}, 0\right) \tag{2.114}$$

$$F_{turb} = e^{-\left(\frac{R_T}{2}\right)^4} \tag{2.115}$$

$$R_T = \frac{\rho k}{\mu\omega} \tag{2.116}$$

$$Re_\nu = \frac{\rho d_w^2 S}{\mu} \tag{2.117}$$

$$Re_{\theta c} = f\left(Tu_L, \lambda_{\theta L}\right) \tag{2.118}$$

In where d_w represents the wall distance and $Re_{\theta c}$ is the critical momentum thickness Reynolds number, whose value can be obtained as:

$$Re_{\theta c}\left(\lambda_{\theta L}, Tu_L\right) = C_{TU1} + C_{TU2}e^{\left[-C_{TU3}Tu_L F_{PG}\left(\lambda_{\theta L}\right)\right]} \tag{2.119}$$

On that equation, $\lambda_{\theta L}$ and Tu_L are two locally defined values employed to approximate the pressure gradient and the freestream turbulence intensity respectively [22]:

$$\lambda_{\theta L} = -7.57 \cdot 10^{-3}\frac{dV}{dy}\frac{d_{w^2}}{\nu} + 0.0128 \tag{2.120}$$

$$Tu_L = min\left(100\frac{\sqrt{2k/3}}{\omega d_w}, 100\right) \tag{2.121}$$

In the case of the $\lambda_{\theta L}$ parameter, its value is limited in order to obtain higher numerical robustness:

$$\lambda_{\theta L} = min\left(max\left(\lambda_{\theta L}, -1.0\right), 1.0\right) \tag{2.122}$$

Moreover, in equation 2.119 the function F_{PG} represents the pressure´s gradient influence on transition and it´s value can be calculated as [22]:

$$F_{PG}\left(\lambda_\theta\right) = \begin{cases} min\left(1 + C_{PG1}\lambda_\theta, C_{PG1}^{lim}\right) & \text{for } \lambda_\theta \geq 0 \\ min\left(1 + C_{PG2}\lambda_\theta + C_{PG3}min\left[\lambda_\theta + 0.0681, 0\right], C_{PG2}^{lim}\right) & \text{for } \lambda_\theta < 0 \end{cases} \tag{2.123}$$

Through out the model, different constants are employed. The following list summarizes the use of each of them [22]:

- C_{TU1} is the minimum value of $Re_{\theta c}$
- $C_{TU1} + C_{TU2}$ is the maximum value of $Re_{\theta c}$
- C_{TU1}, is a parameter employed to command the $Re_{\theta c}$ decrease caused by the turbulence intensity (Tu) increment.
- C_{PG1} and C_{PG2} are employed to adjust the $Re_{\theta c}$ when modelling areas with adverse and favorable pressure gradient.

- C_{PG3} is employed to modify the $Re_{\theta c}$ value only in some cases where separation exists.
- C_{PG1}^{lim} and C_{PG2}^{lim} are employed to set the F_{PG} function´s limits.

Coupling the intermittency transition model with the STT model, it is obtained that:

$$\frac{\partial}{\partial t}(\rho k)+\frac{\partial}{\partial x_j}(\rho u_j k)=\widetilde{P_k}+P_k^{lim}-\widetilde{D_k}+\frac{\partial}{\partial x_j}\left((\mu+\sigma_k\mu_t)\frac{\partial k}{\partial x_j}\right) \tag{2.124}$$

$$\frac{\partial}{\partial t}(\rho \omega)+\frac{\partial}{\partial x_j}(\rho u_j \omega)=\alpha\frac{P_k}{\nu_t}-D_\omega+Cd_\omega+\frac{\partial}{\partial x_j}\left((\mu+\sigma_\omega\mu_t)\frac{\partial \omega}{\partial x_j}\right) \tag{2.125}$$

$$\widetilde{P_k}=\gamma P_k \tag{2.126}$$

$$\widetilde{D_k}=max\left(\gamma,0.1\right)\cdot D_k \tag{2.127}$$

In where P_k and D_k are the production and destruction terms in the SST turbulent kinetic energy equation. In addition, for the analyzed problem, a new term, P_k^{lim},is included to guarantee correct generation of **k** in transition when Tu is in low levels (close to zero). It´s value can be obtained as:

$$P_k^{lim}=5C_k max\left(\gamma-0.2,0\right)\left(1-\gamma\right)F_{on}^{lim} max\left(3C_{SEP}\mu-\mu_t,0\right)S\Omega \tag{2.128}$$

$$F_{on}^{lim}=min\left(max\left(\frac{Re_\nu}{2.2Re_{\theta c}^{lim}}-1,0\right),3.0\right) \tag{2.129}$$

$$Re_{\theta c}^{lim}=1100 \tag{2.130}$$

$$C_k=1.0, C_{SEP}=1 \tag{2.131}$$

The C_{SEP} is an adjustable parameter that allows the control of the bubble´s separation size when the laminar boundary layer splits and whose value is set to 1 as default.

2.6 Non-dimensional Numbers

In fluid mechanics, the dimensionless parameters are useful to calculate the flow properties of a fluid. In order to understand the fluid behaviour as well as to extrapolate one problem to another of larger or smaller scale, a study of this parameters is recommended. The following pages summarize the most relevant non-dimensional parameters employed in this project.

2.6.1 Reynolds Number

The Reynolds Number, whose value can be estimated by equation 2.132, establishes the relation between the viscous and inertial forces and describes the fluid flow behaviour. Thereby, if the inertial forces are larger than the viscous forces, the flow will behave as turbulent, where as if the inertial forces are smaller than viscous forces, the flow will be laminar.

$$Re = \sqrt{\frac{InertialForces}{ViscousForces}} = \frac{\rho u d}{\mu} \tag{2.132}$$

In where ρ is the fluid density, μ is the fluid dynamic viscosity and u is the fluid velocity. Moreover, the parameter d represents the characteristic length and its value can differ depending on the analyzed case, being the diameter in the case of a circumferential tube, the length in a flat plate case, or the hydraulic diameter (D_h) in complex geometries.

$$D_h = \frac{4A}{P} \tag{2.133}$$

Where P is the wetted perimeter and A the cross-sectional area.

2.6.2 Prandtl Number

Prandtl Number is a non-dimensional parameter that relates the momentum diffusivity (kinematic viscosity) with the thermal diffusivity being only dependent on the fluid properties. Moreover, it´s a parameter mainly used in heat transfer and convection applications.

$$Pr = \frac{\nu}{\alpha} \tag{2.134}$$

2.6.3 Nusselt Number

Due to the fact that Nusselt number measures the convection heat transfer on a surface, this non-dimensional parameter is of great importance in heat transfer applications. Moreover, if the Nusselt number is known, the heat transfer coefficient can be directly estimated [23].

$$Nu = \frac{ConvectiveHeatTransfer}{ConductiveHeatTransfer} = \frac{hL}{k_{fluid}} \tag{2.135}$$

Different approaches have already been developed to calculate the value of the Nusselt number, being all of them dependent on the Prandtl number, Reynolds number and dimensionless distance.In addition, the most common boundary conditions are, uniform wall heat flux (UHF) and uniform wall temperature (UWT).

2.6.3.1 Flat Plate Correlations

For external forced flow, the local Nusselt number correlation for constant wall temperature is:

Laminar flow:

$$Nu_x = 0.332 Re_x^{\frac{1}{2}} Pr^{\frac{2}{3}} \quad for\ 0.6 \leq Pr \tag{2.136}$$

Averaged:

$$\overline{Nu_L} = 0.664 Re_L^{\frac{1}{2}} Pr^{\frac{1}{3}} \tag{2.137}$$

Turbulent:

$$Nu_x = 0.0296 Re_x^{\frac{4}{5}} Pr^{\frac{1}{3}} \quad for\ 0.6 \leq Pr \leq 60 \tag{2.138}$$

Averaged:

$$\overline{Nu_L} = 0.037 Re_L^{\frac{4}{5}} Pr^{\frac{1}{3}} \tag{2.139}$$

For $0.6 \leq Pr \leq 60$ and $5 \cdot 10^5 \leq Re_L \leq 10^7$

In the case of mixed region, the averaged Nusselt correlation at constant wall temperature is [24]:

$$\overline{Nu_L} = \left(0.037 Re_L^{\frac{4}{5}} - A\right) Pr^{\frac{1}{3}} \tag{2.140}$$

$$A = 0.037 Re_{x,c}^{\frac{4}{5}} - 0.664 Re_{x,c}^{\frac{1}{2}} \tag{2.141}$$

For $0.6 \leq Pr \leq 60$ and $Re_{x,c} \leq Re_L \leq 10^8$

Furthermore, the previous stated equations can be combined in order to obtain the local Nusselt number when considering the transition region [24]:

Laminar Region

$$Nu_{laminar}(Re_x, Pr) = \begin{cases} 0.332 Re_x^{\frac{1}{2}} Pr^{\frac{1}{3}} & UWT \\ 0.453 Re_x^{\frac{1}{2}} Pr^{\frac{1}{3}} & UHF \end{cases} \tag{2.142}$$

Transition Region

$$Nu_{trans} = Nu_{lam}\left(Re_l, Pr\right)\left(\frac{Re_x}{Re_l}\right)^c \tag{2.143}$$

$$Re_l = 3.5 \cdot 10^5 \left(\frac{100u_r'}{u_\infty}\right)^{-\frac{5}{4}} \tag{2.144}$$

$$c = 0.9955 log_{10} Re_l - 3.013 \tag{2.145}$$

For $Re_l < 5 \cdot 10^5$

Turbulent Region

$$Nu_{turb} = \frac{Re_x Pr\left(\frac{C_f}{2}\right)}{1 + 12.7\left(Pr^{\frac{2}{3}} - 1\right)\sqrt{\frac{C_f}{2}}} \tag{2.146}$$

$$C_f = \frac{0.455}{\left[ln\left(0.06 Re_x\right)\right]^2} \tag{2.147}$$

In the case of working with gases, the previous expression can be simplified:

$$Nu_{turb} = 0.0296 Re_x^{0.8} Pr^{0.6} \tag{2.148}$$

$$Nu_x = \left[Nu_{lam}^5 + \left(Nu_{trans}^{-10} + Nu_{turb}^{-10}\right)^{\frac{-1}{2}}\right]^{\frac{1}{5}} \tag{2.149}$$

Correlations for external flow need to be modified in order to account the significant variation on the fluid properties. To do so, the flow is evaluated at the freestream temperature (T_∞), thereby, result need to be corrected by multiplying it by the absolute temperature ratio $\left(\frac{Tw}{T_\infty}\right)^{-n}$ in which n is in the range of 0.25 to 0.4 [24].

3

Methodology

3.1 Geometry

This project has been developed by means of CFD simulations of the 2.5 stage low pressure compressor whose geometry, main properties and design point operation conditions are schematized in figure 3.1 and table 3.1.

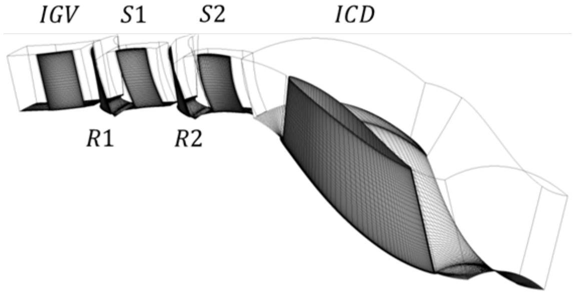

Figure 3.1: ENABLEH2 compressor geometry. The geometry is composed of an Inlet Guide Vane (IGV), Rotor 1 (R1), Stator 1 (S1), Rotor 2 (R2), Stator 2 (S2), and an Intermediate Compressor Duct (ICD)

ENABLEH2 Compressor	
Rotational Speed	1920 rpm
Mass flow	17 kg/s
Pressure ratio	1.07
Tip Speed	100 m/s
Axial Velocity 70 m/s	
Rotor Re_c	600 000
Avg Tip radius	620 mm
Avg Hub radius	540 mm
N. stator Blades (IGV, S1, OGV, ICD)	75, 126, 124, 8
N. rotor Blades (R1, R2)	61, 69
Avg Aspect Ratio	2.157
Avg Tip Clearance	0.75 mm

Table 3.1: ENABLEH2 compressor properties and design operating point [25]-[26].

This compressor, which will be referred in this document as the ENABLEH2 compressor, is used for experimental purposes and was designed with the goal of replicating the last stages of a modern high-speed LPC in the virtual engine VINK [27].

Specifically, the simulations carried out in this project will focus on the the ICD, whose geometry can be seen in figure 3.2.

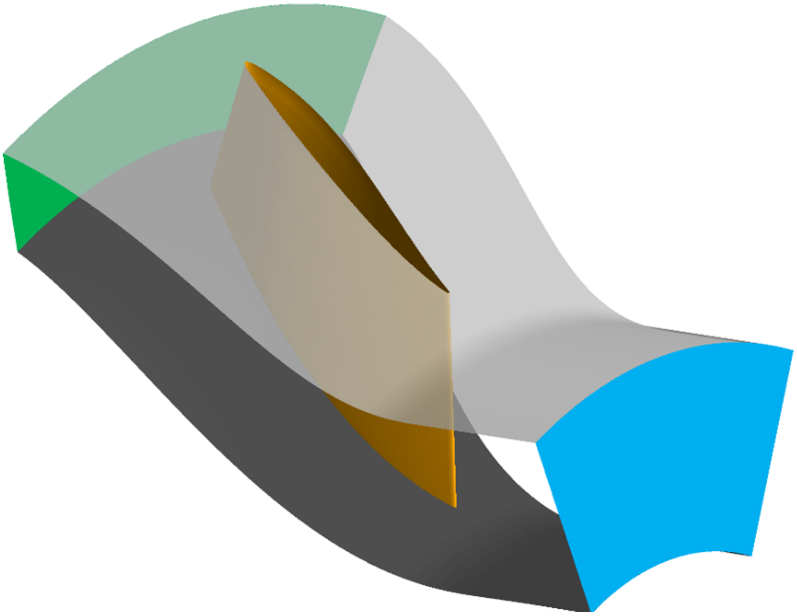

Figure 3.2: ICD geometry: Vane surface (orange), hub (dark grey), shroud (light grey), inlet (green), and outlet (blue). Periodic surfaces not explicitly shown.

3.2 Mesh

To carry the mesh study, ANSYS R1 2021 is employed, specifically, the turbomachinery blade meshing software, Turbogrid. In the case of this project, the meshing will be focused on the ICD as well as in the vane, STRUT, located on it.

Different sets can be applied to generate the meshes by modifying the "Mesh data" tab in the software. In order to define the mesh size, two different methods exists: *'Global Size Factor'* which enables the user to define the overall mesh size and the *'Target Passage Mesh Size'* in which the number of nodes in the mesh can be selected between 'Fine' (250000), 'Medium'(100000), 'Coarse' (20000) or 'Specify'. The Target Passage Mesh Size is the employed method in the mesh study where the number of cells will be varied from 750K up to 10M cells. Increasing the number of cells in the mesh will end up in higher accuracy, however, the computational cost will also increase, thus, a balance between simulation time and accuracy of the results must be assured.

In order to solve the boundary layer and thereby model the fluid´s heat transfer behaviour, it is necessary to carefully define the mesh near the wall. To control the boundary layer distribution three variables need to be tracked, these are: the number of elements across the boundary region, thus, the width of the layers, the expansion rate, which represents how the layers height increase while the distance from the wall increases, and the first element offset, which represents the height of the first layer next to the wall. To do so, the employed software uses the "Boundary Layer Refinement Control" tool.

The previous mentioned tool,"Boundary Layer Refinement Control" has two different configurations: the 'Proportional to Mesh Size' and the 'First Element Offset'. While the first choice calculates the number of elements in the boundary layer as a function of new different factors such as the 'Factor Ratio' or 'Factor Base', the second choice directly measures the first row of cells adjacent to the blade. Between these two methods, the employed in the project is the 'First Element Offset' as it assures obtaining the desired $y^+ < 1$. To calculate the offset, an iterative process has been followed, leading to a final value of $1 \cdot 10^{-6}$ based on experienced gained in previous simulations.

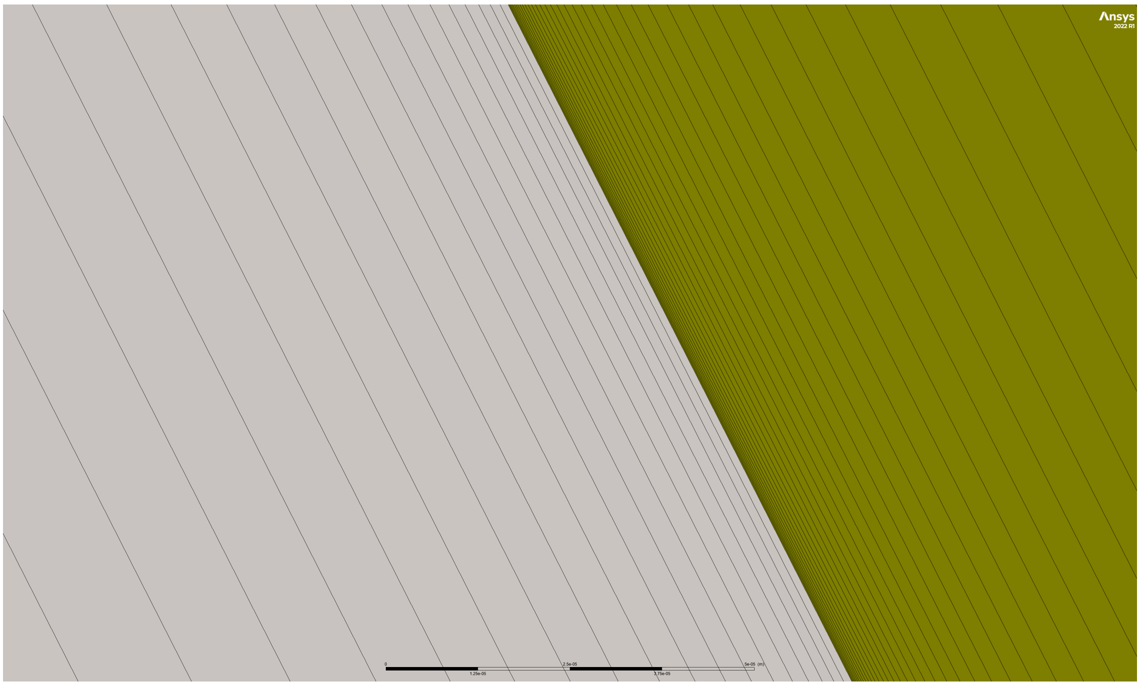

Figure 3.3: Hub Mesh Boundary Layer close to the vane

Another tab that must be selected during the mesh set up, is the 'Target Maximum Expansion Rate'. This tool avoids getting expansion rates larger than the maximum specified ones. When using the 'First Element Offset', it is necessary to increase the number of elements in the boundary layer to thereby reduce the highest expansion rate. In this project, this parameter is set to 1.2 based on previous experience.

After all, the mesh turns out to be as shown in the following figures :

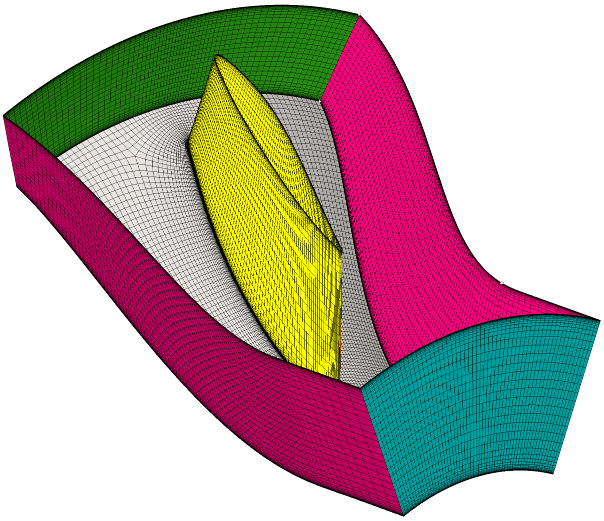

Figure 3.4: ICD mesh without the shroud.

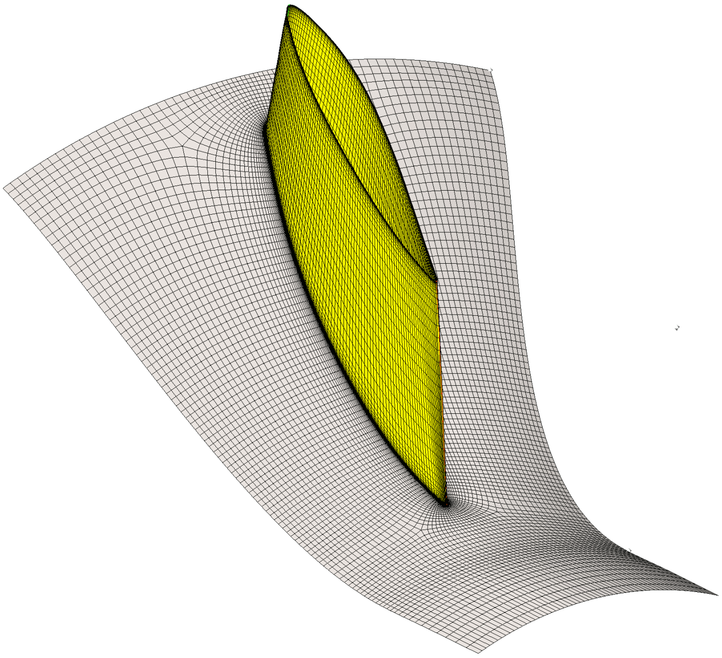

Figure 3.5: Hub and vane mesh.

3.3 Numerical set up

Once the geometry and mesh have been developed, it is necessary to define the fluid and domain properties. To do so, CFX-Pre is employed [28].

Regarding to the fluid properties, the following settings have been applied. Firstly, the fluid has been defined to be "Air Ideal Gas", thus, the ideal gas equation is employed to calculate the density with a default molar mass of 28.96 $kg/kmol$. Moreover, a value of 1004.4 J/kgK is employed to define the 'Specific Heat Capacity' at constant pressure. Regarding to the reference properties, 25 °Cand 1 atm are respectively selected for temperature and pressure where as no reference values are defined for both the entalphy and entropy. In the case of the transport properties, the fluid has been defined to have a constant dynamic viscosity of $1.831{\cdot}10^{-5} kg/(ms)$ and a constant thermal conductivity of 0.0261 W/(mK). However, it should be noted that fluid properties will be considered to be variable when studying the effect of temperature on the transition as explained in section 3.3.2. Finally, regarding to the radiation properties, default settings are considered, thus, a refractive index of 1 , an absorption coefficient of 0.01 and a scattering coefficient of 0 have been considered.

In the case of the ICD, as the fluid will flow through it, the domain has been defined as "Fluid Domain", using the previous explained 'Air Ideal Gas' as the employed material with a *Continuous Fluid* morphology. In relation with the domain model, the following features have been defined: 0 Pa as the 'Reference Pressure', none buoyant as 'Buoyancy Model', stationary as 'Domain Motion' as well as no 'Mesh Deformation'.

For the ICD heat transfer modelling, the 'Fluid Models' tab offers different choices. These are: *Isothermal*, employed to analyze the fluid properties behaviour in relation with temperature, *Total Energy*, which considers kinetic energy and entalphy effects and *Thermal Energy* which is equivalent to total energy but without considering kinetic energy effects. In this project, the *Total Energy* choice, taking into account the "Viscous Work Term", is employed.

Furthermore, regarding to the "Turbulence", the "Shear Stress Transport" (SST) model as well as the "Gamma Theta" and the "Intermittency" models are employed to model transition.

Finally, to initialize the domain, a constant temperature of 288.15 K is defined and medium intensity is considered for the turbulence.

Afterwards, it is necessary to define the boundary conditions for the 5 different surfaces in the network. For setting the inlet boundary condition, a simulation of the complete ENABLEH2 compressor at the design operating point was performed. As a result, a velocity, pressure, temperature, turbulent kinetic energy and turbulence eddy frequency profile distribution at the inlet of the ICD was obtained. The inlet boundary condition featured an average total pressure and temperature of 102021 Pa and 294.7 K while the average turbulence intensity is 4.8%. The outlet was specified as a static pressure outlet with a pressure of 1 bar, which resulted in matching the design point massflow.

On the other hand, STRUT, hub and shroud have been defined as walls with smooth roughness and no slip, so that the wall and fluid velocity are equal. However, while the hub and shroud are set to be adiabatic, in the case of the STRUT, it is necessary to establish a heat transfer boundary condition for the purpose of analyzing the heat transfer on it. To do so, an outside temperature of 305.15 K, and a constant heat transfer coefficient of 53.59 $\frac{W}{m^2K^{-1}}$, whose value is obtained as explained in section 3.3.1, have been employed.

In addition, with the goal of setting a boundedness criteria, high resolution is selected in the solver control as well as a fluid auto-time scale. For the converge control a maximum of 700 iterations has been set and a convergence criteria in which residuals have to be around $1 \cdot 10^{-6}$.

3.3.1 Boundary Condition for analyzing the vane wall heat transfer.

In the real process the idea is to have a hot fluid, air, flowing trough the ICD and a cold fluid, hydrogen, flowing inside the vane while cooling it. However, the simulations will be characterized to instead have an equivalent heat transfer process in where warm water at 32°C circulates inside the vane heating it and thereby, providing a warm heat flux to the outside colder flow.

Moreover, as stated before, in view of modelling the heat transfer along the vane, a constant heat transfer coefficient needs to be defined. To obtain that value, a complex 3D-heat transfer problem needs to be solved. However, the process can be simplified leading to the one-dimensional approach shown on figure 3.6.

If the thermal resistance method (section 2.3) is applied between the water and the vane, the heat flux per unit of area in the Strut can be calculated by the following equations:

$$q'' = \frac{T_{s1} - T_{\infty 2}}{R''_{BC}} \tag{3.1}$$

$$R''_{BC} = \frac{L}{k} + \frac{1}{h_{conv,2}} \tag{3.2}$$

Where subindex 1 relates to the vane wall, subindex 2 to the warm water and subindex "BC" to the heat transfer boundary condition applied in CFX.

On one hand, to define the length of the vane, a value of 4 mm has been selected as it is the minimal wall thickness that could be manufactured using modern SLA

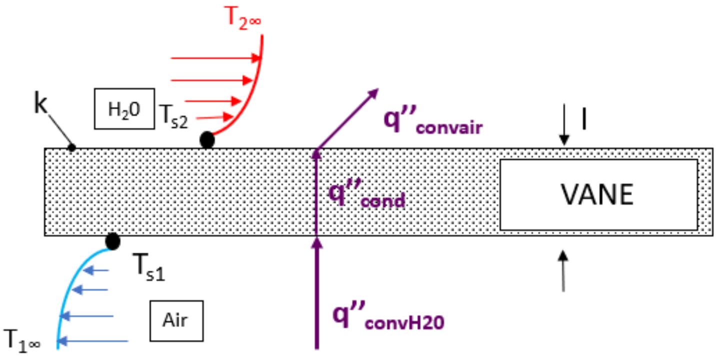

Figure 3.6: One-dimensional approach of the vane heat transfer process

printers within acceptable uncertainty of 2% [29]. In the case of the vane´s thermal conductivity, a value of 0.2175 W/mK has been selected based on the measures carried out by HotDisk AB following ISO22007-2 [30].On the other hand, the convection heat transfer coefficient for the water is obtained from previous works leading to a value of 3700 W/m^2K [29].

As a result, the desired thermo-resistance can be calculated:

$$R''_{BC} = \frac{L}{k} + \frac{1}{h_{conv,2}} = \frac{4 \cdot 10^{-3}}{0.2175} + \frac{1}{3700} = 0.0186\ \frac{m^2K}{W} \tag{3.3}$$

However, CFX does not allow directly using the thermo-resistance as a boundary condition, instead, it uses the overall heat transfer coefficient, which is the inverse value of the previously calculated resistance. Thereby, a value of 53.59 W/m^2K for the heat transfer coefficient is employed.

3.3.2 Boundary and Operation Conditions to estimate the effect of wall temperature in transition

With the goal of analyzing the effect of cooling/heating the vane into the transition region, 6 simulations will be carried at different constant and decreasing temperatures. To do so, instead of setting a constant heat transfer coefficient in the vane, a constant temperature in the strut will be used as boundary condition.

When working under high temperature ranges between the freestream and the wall, important variations of the results as well as more complex simulations are obtained. To avoid so, and taking into account that fluid properties such as thermal conductivity (k), dynamic viscosity (μ) and the specific heat capacity at constant pressure (cp) play an important role on the heat transfer governing equations, it is necessary to model the behaviour of the flow properties.

To do so, the software REFPROP is employed to produce air thermophysical data at ambient pressure, in the temperature range between 90-400K [31]. Subsequently, Python is used to obtain polynomials that model the trend and behavior of each of the thermophysical properties in the data base with minimal error. Moreover, the obtained polynomials are only temperature dependent due to the fact neither the simulated problem nor the modelled properties have a big dependency on pressure.

The polynomials finally employed are of 8^{th} order and on them the temperature is expressed on Kelvin. In addition, while for both the thermal conductivity and the dynamic viscosity the obtained expressions have an error below 0.005%, in the case of the specific capacity at constant pressure, the error is below 0.08 %.

The following pages show, for each of the fluid properties considered, the polynomial expression as well as a graphical comparison between the behaviour of the polynomial (pink) and the REFPROP data (blue).

Dynamic Viscosity (μ)

$$\begin{aligned}\mu = (&-7.7152519\cdot 10^{-1} + 8.943062\cdot 10^{-2}T - 1.382705c\dot{1}0^{-4}T^2 + 3.615254\cdot 10^{-7}T^3 \\ &- 1.343618\cdot 10^{-9}T^4 + 4.571345\cdot 10^{-12}T^5 - 1.026955\cdot 10^{-14}T^6 + 1.288594\cdot 10^{-17}T^7 \\ &- 6.830077\cdot 10^{-21}T^8)\cdot 10^{-6} \quad Pa\ s\end{aligned} \tag{3.4}$$

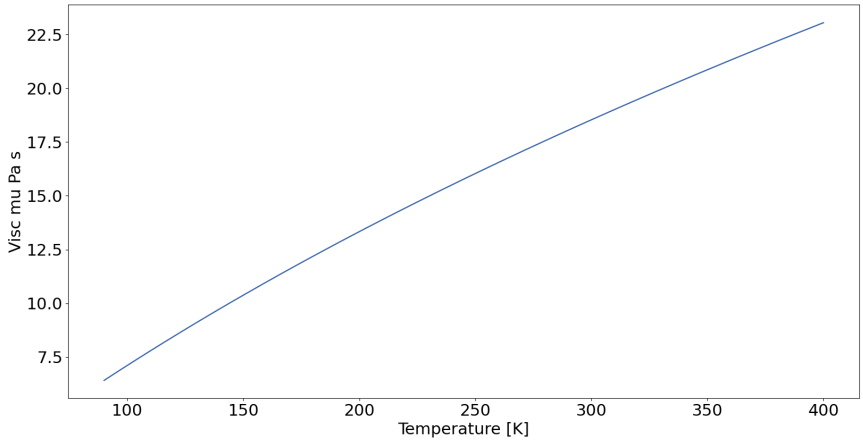

Figure 3.7: Modeling of the dynamic viscosity (Pa s) for temperatures between 90-400K

Thermal Conductivity (k)

$$\begin{aligned}k = (&-3.970531\cdot 10^{-2} + 7.788963\cdot 10^{-2}T + 4.434811\cdot 10^{-4}T^2 - 4.345211\cdot 10^{-6}T^3 \\ &+ 2.204929\cdot 10^{-8}T^4 - 6.929422\cdot 10^{-11}T^5 + 1.339884\cdot 10^{-13}T^6 - 1.459909\cdot 10^{-15}T^7 \\ &+ 6.860295\cdot 10^{-20}T^8)\cdot 10^{-3} \quad \frac{W}{mK}\end{aligned} \tag{3.5}$$

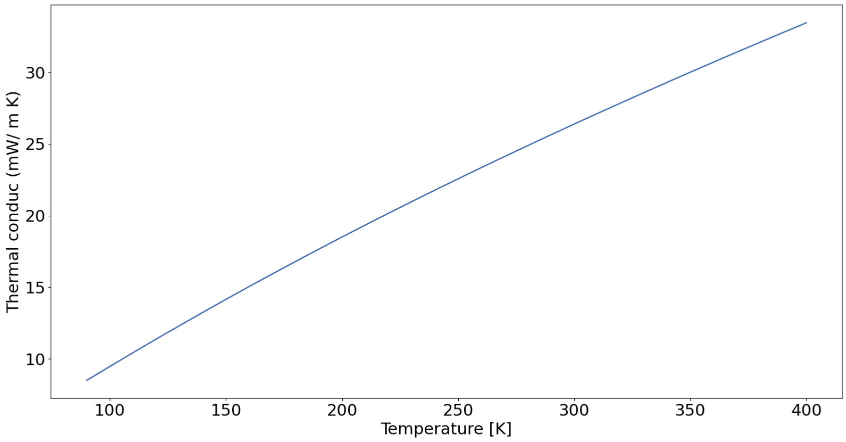

Figure 3.8: Modeling of the thermal conductivity (mW/mK) for temperatures between 90-400K

Specific Heat Capacity at constant pressure (cp)

$$cp = (2.786061 \cdot 10^{3} - 5.885736 \cdot 10^{1} T + 8.545620 \cdot 10^{-1} T^{2} - 7.036793 \cdot 10^{-3} T^{3} + 3.573300 \cdot 10^{-5} T^{4} - 1.142807 \cdot 10^{-7} T^{5} + 2.245610 \cdot 10^{-10} T^{6} - 2.478127 \cdot 10^{-13} T^{7} + 1.176146 \cdot 10^{-16} T^{8}) \quad \frac{J}{kgK} \tag{3.6}$$

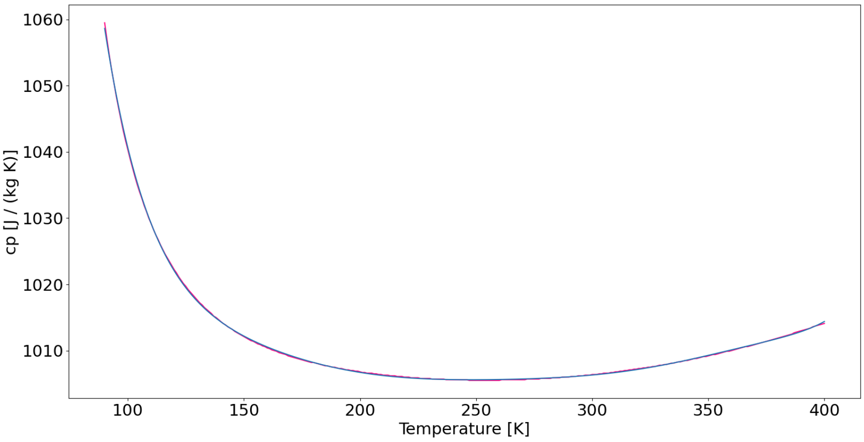

Figure 3.9: Modeling of the specific capacity at constant pressure (J/kgK) for temperatures between 90-400K

4

Results

4.1 Mesh Independence Study

As explained before, the finer the mesh, the higher accuracy and quality in the results. However, the use of finer meshes leads to longer solving times, thus, higher computational costs. As a result of this, a balance between accuracy and computational cost needs to be ensured. To do so, a mesh independence study has been carried out for the two transition models employed in the project.

The mesh independence study, whose results are summarized for each of the transition models in tables 4.1 and 4.2, consists of 6 distinct cases with mesh cell counts ranging from 750 000 to 10 million cells. Furthermore, all 6 cases, which hold a first node height below $y^+ = 1$, were refined by setting a target passage mesh cell count in ANSYS Turbogrid so that a global refinement in all directions of the mesh was reached.

In order to control the process while running and thereby be able to compare the accuracy and convergence of the results, 4 different control parameters have been defined. These are: the pressure loss (Δp) and total enthalpy change (Δh_0), which have been calculated from the inlet to outlet, as well as the pressure ratio (r) and the heat flow q_{vane}, which has been calculated as the area integral of the heat flux along the surface of the vane.

Case	Ncells [10^6]	ΔP (%)	r (%)	Δh (%)	q_{vane} (%)
Mesh 1	0.75	9.50	-0.01	23.16	1.04
Mesh 2	1	7.25	-0.01	18.57	0.68
Mesh 3	2	3.89	0.00	8.72	0.29
Mesh 4	5	1.15	0.00	3.35	0.15
Mesh 5	7.5	0.57	0.00	1.11	0.10
Mesh 6	**10**	**0.00**	**0.00**	**0.00**	**0.00**

Table 4.1: Mesh study for the ICD using the Gamma-Theta Transition Model. All changes are relative to case 6 (bold).

Case	Ncells [10^6]	ΔP (%)	r (%)	Δh (%)	q_{vane} (%)
Mesh 1	0.75	9.10	-0.01	23.22	1.03
Mesh 2	1	8.72	-0.01	19.57	0.70
Mesh 3	2	4.48	0.00	9.46	0.24
Mesh 4	5	0.85	0.00	2.88	0.12
Mesh 5	7.5	0.63	0.00	0.90	0.04
Mesh 6	**10**	**0.00**	**0.00**	**0.00**	**0.00**

Table 4.2: Mesh study for the ICD using the Intermittency Transition Model. All changes are relative to case 6 (bold).

From results it can be observed that the total enthalpy change (Δh_0) from inlet to outlet varies significantly between the 6 cases, especially in comparison to the vane heat flow (q_{vane}). This discrepancy is thought to be a result of different factors. Firstly, it is considered that the discrepancy may be linked to the global domain imbalance of the energy equation as well as to the overall convergence. Global imbalance is influenced by the numerical accuracy of the results due to the small amount of heat being transferred in the vane in comparison to the enthalpy flow in both inlet and outlet. However, the discrepancy could also be influenced by the two hub separations that exist on each side of the vane (Figure 4.1) which could potentially decrease convergence of the results due to its transient nature.

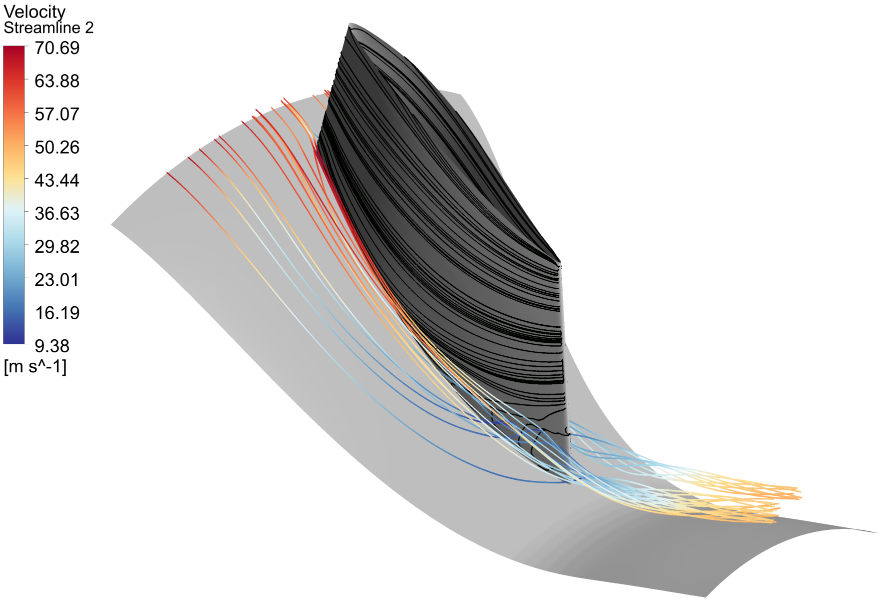

Figure 4.1: Surface streamlines on the ICD vane showing a hub separation and the two accompanying vortices being convected downstream

For both transition models it was seen that case 6, with 10 million cells, was accurate enough as it had normalized differences in the order of 1 % relative to the second finest mesh. As a result, it was deemed to be the most adequate mesh definition to represent the heat transfer in the flow. Also, the finer meshes yielded to better convergence and lower global imbalances, thus, Δh_0 approached the value q_{vane}.

Another relevant conclusion obtained from the mesh study was that finer meshes lead to more delayed onsets as well as to longer transition regions.This behaviour can be observed in figure 4.2 for both the Gamma Theta and Intermittency transition model.

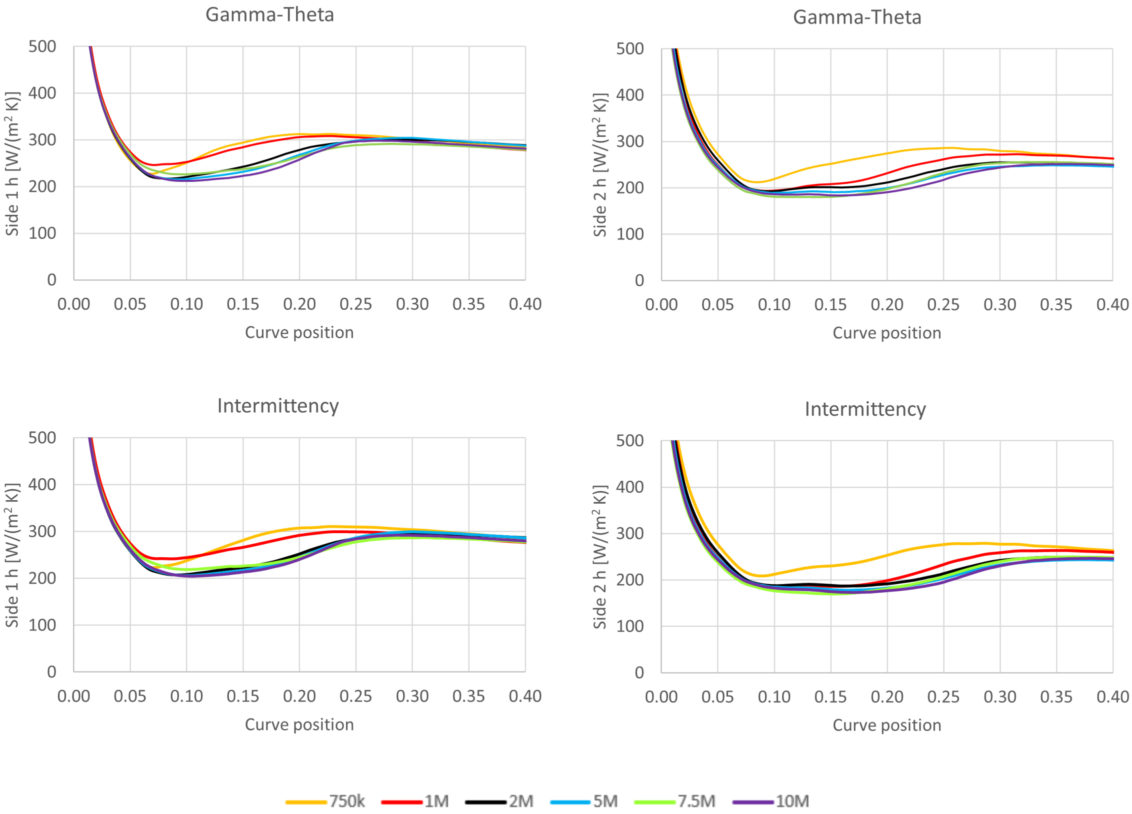

Figure 4.2: Heat transfer coefficient h at midspan for side 1 (left) and side 2 (right) of the ICD vane for both the Gamma-Theta (top) and Intermittency (bottom) transition models for the different cases used in the mesh study. The y and x-axis have been capped to improve readability.

For the finest mesh, that is, the 10 million cells case, transition from laminar to turbulent boundary layer is shown for the vane in terms of turbulent kinetic energy and convective heat transfer coefficient. Both properties show that, when the Gamma-Theta Model is considered and a constant heat transfer coefficient of 53.59 W/m^2K is defined along the vane, transition occurs at approximately 20% of the vane´s chord:

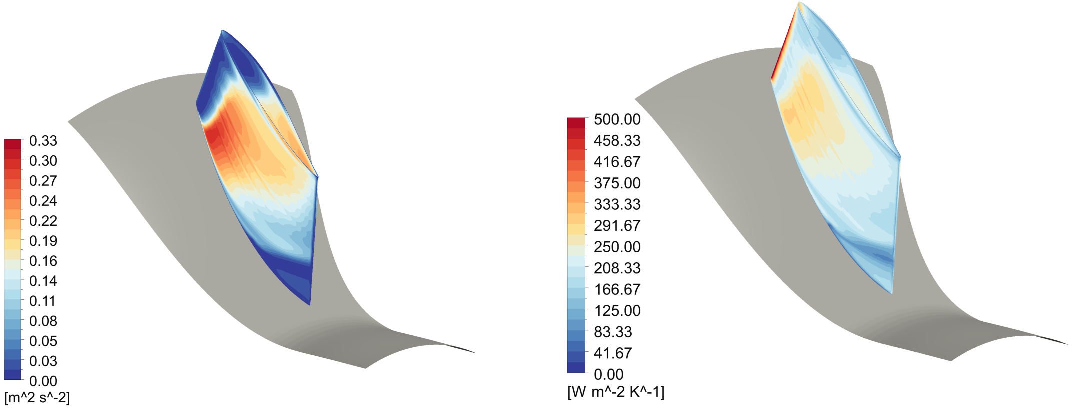

(a) **(b)**

Figure 4.3: For the Gamma-Theta transition model: a) Turbulent kinetic energy on the vane surface, b) Convective heat transfer coefficient on the vane surface.

Focusing on the convective heat transfer coefficient along the vane, the value in figure 4.3b is capped at 500 W/(m^2 K) in order to improve readability.However, values of 900 W/(m^2 K) are reached at the leading edge of the vane: (Figure 4.4).

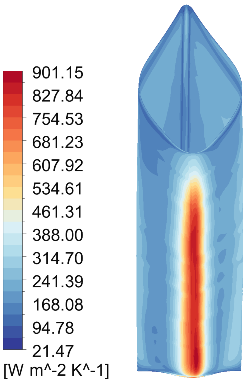

Figure 4.4: Convective Heat Transfer coefficient at the leading edge of the vane for the Gamma-Theta transition model

Similar results and conclusions are reached for the intermittency transition model:

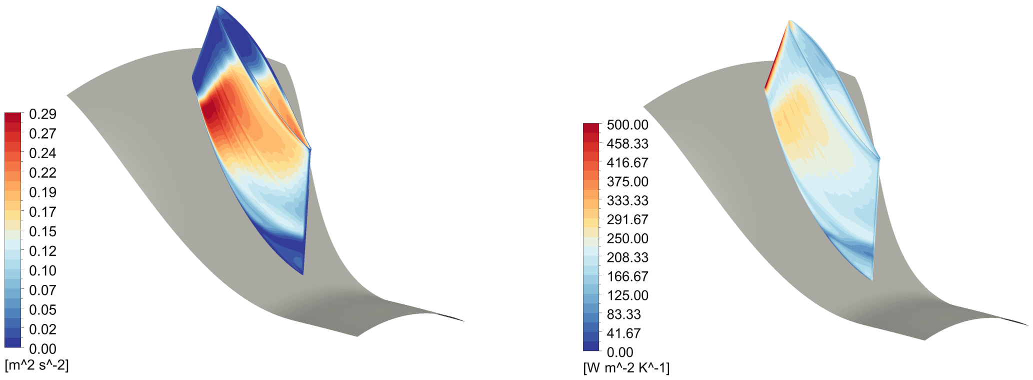

(a) **(b)**

Figure 4.5: For the intermittency transition model: a) Turbulent kinetic energy on the vane surface, b) Convective heat transfer coefficient on the vane surface.

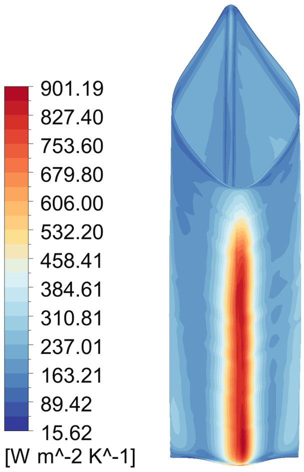

Figure 4.6: Convective Heat Transfer coefficient at the leading edge of the vane for the Intermittency transition model

4.2 Effect of wall temperature in transition

In order to analyze the effect of cooling in the transition region, a parametric study has been carried out for both transition models. To do so, 5 different simulations, each of them with 5 different and decreasing constant wall temperatures, have been performed.

For both transition models the behaviour of the heat transfer coefficient at each side of the vane has been calculated. As a result, figures 4.7a, 4.7b, 4.7c and 4.7d are obtained. Here it can be observed that both transition models lead to similar transition behaviours as well as to almost equal results.

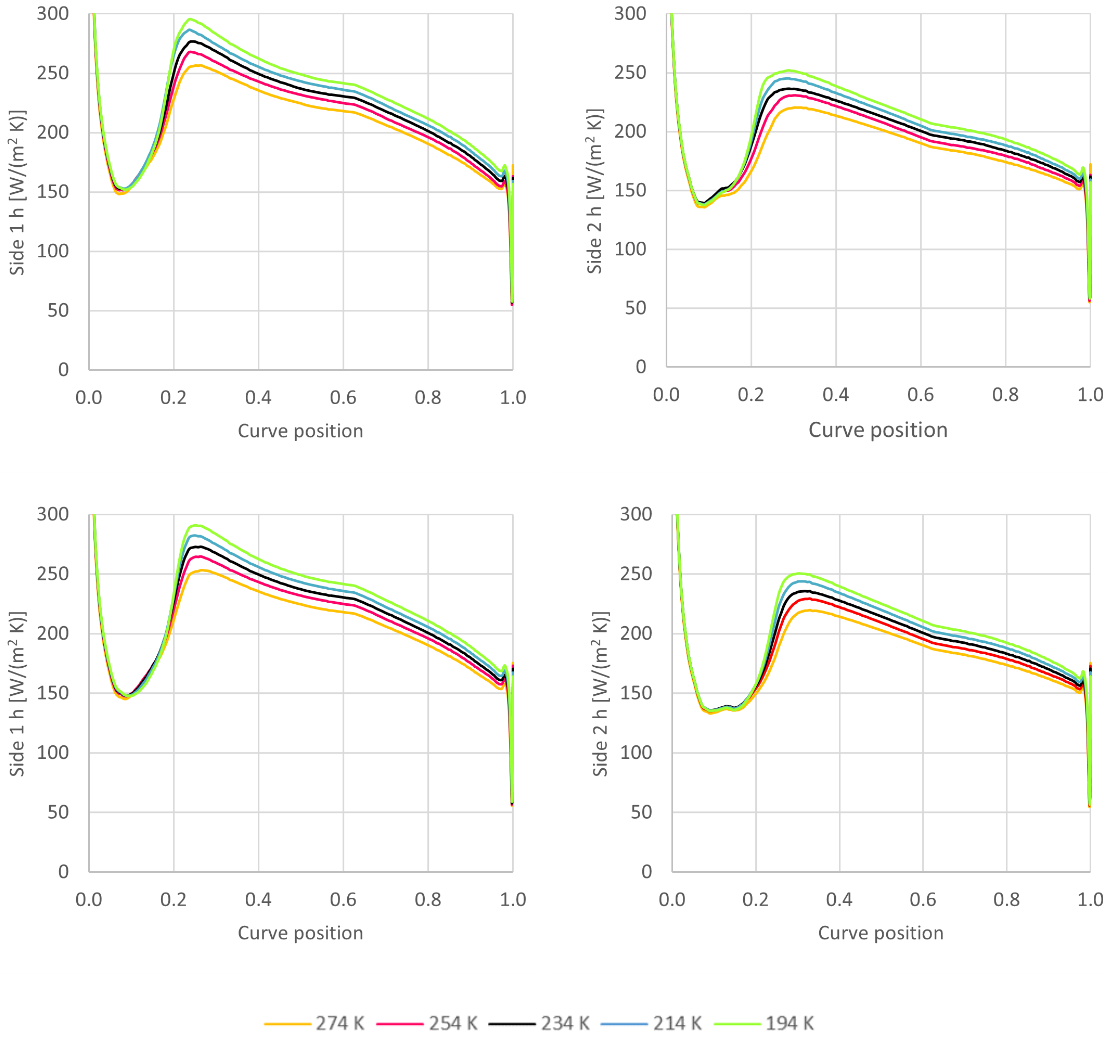

Figure 4.7: Heat transfer coefficient h at midspan for side 1 (left) and side 2 (right) of the ICD vane for both the Gamma-Theta (top) and Intermittency (bottom) transition models for the different cases used in the parametric study.

Transition seems to speed up and move downstream on the vane for lower temperatures. However, this behaviour is difficult to discern graphically from figures above. The Euler-derivative is employed to estimate the inflection points that define the beginning and end of transition. Results, summarized for each model in tables 4.3 and 4.4, are in line with theory ([17]) as they show that cooling leads to more stable boundary layers, thus, higher transition Reynolds numbers.

Case	Temperature (K)	Inflection point	End of transition	Length of transition
T1	274.656	0.0833	0.2631	0.1799
T2	254.656	0.0833	0.2408	0.1575
T3	234.656	0.0874	0.2408	0.1534
T4	214.656	0.0874	0.2398	0.1524
T5	194.656	0.0915	0.2398	0.1483

Table 4.3: Effect of cooling in the transition region for the Gamma-Theta model.

Case	Temperature (K)	Inflection point	End of transition	Length of transition
T1	274.656	0.0874	0.2688	0.1814
T2	254.656	0.0874	0.2631	0.1758
T3	234.656	0.0874	0.2631	0.1758
T4	214.656	0.0915	0.2631	0.1717
T5	194.656	0.0956	0.2631	0.1675

Table 4.4: Effect of cooling in the transition region for the intermittency model.

This tendency was further confirmed after running a case in where heating was modelled. To do so, instead of decreasing the wall temperature in comparison to the average temperature of the flow, as it was done in the previous simulations, the wall temperature was increased up to 394.656 K.

As it can be seen in figure 4.8, when instead of cooling the vane is heated, the transition occurs earlier. This is due to the fact heating processes leads to more unstable boundary layers. Moreover, when heating the vane, the heat transfer coefficient along the vane is reduced.

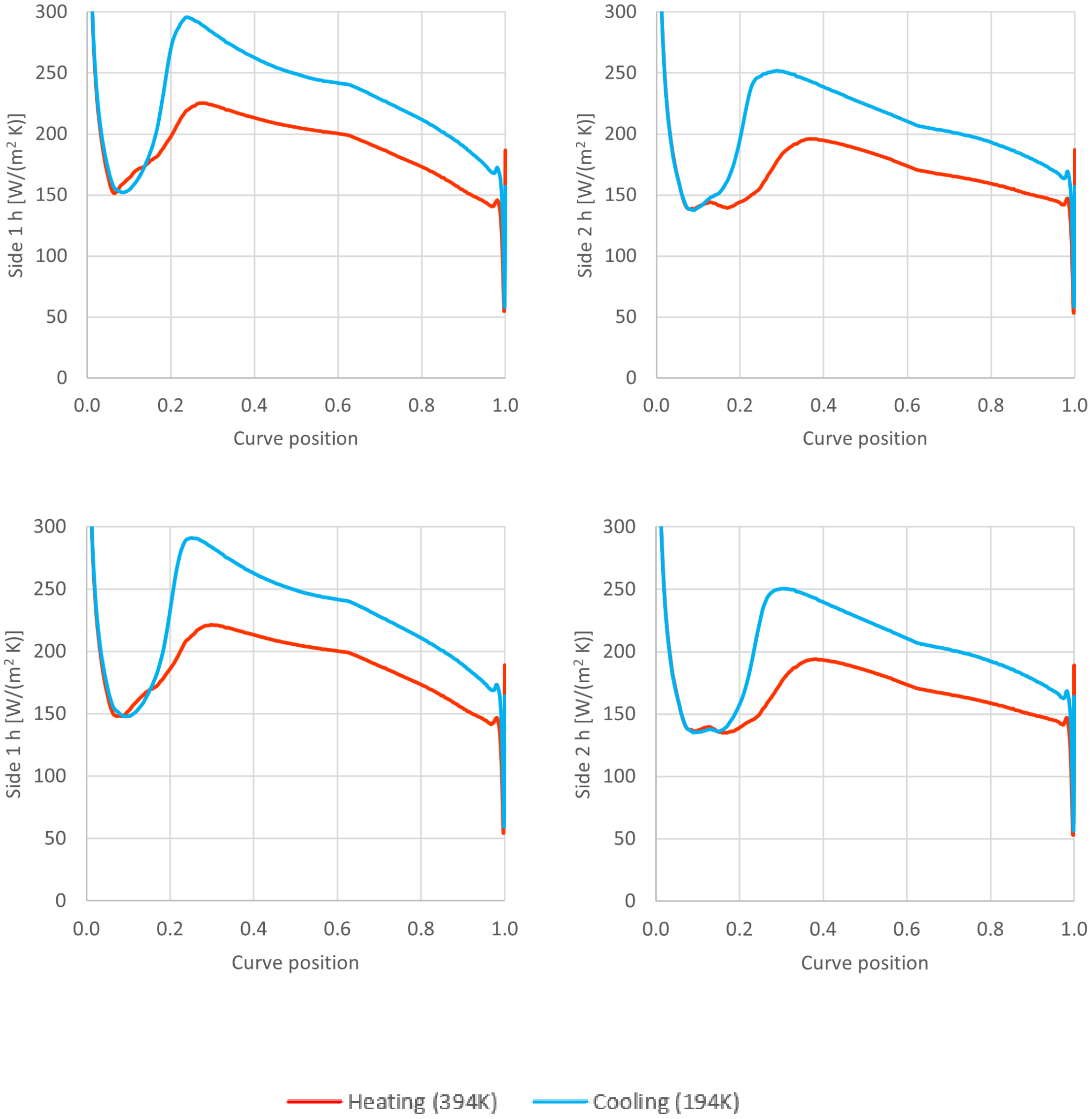

Figure 4.8: Heat transfer coefficient at midspan for side 1 (left) and side 2 (right) of the ICD vane for both the Gamma-Theta (top) and Intermittency (bottom) transition models when cooling (blue) and heating (red)

4.3 Flat Plate Validation

Finally, a flat plate validation of the results has been carried out. To do so, the flat plate correlations explained in section 2.6.3 have been employed. After calculating the Nusselt number for each flow regime, equation 2.135 has been applied to calculate the heat transfer coefficient along the vane.

The results obtained after comparing the case of having a vane with a constant wall temperature of 91K against the correlations are plotted in figure 4.9 and 4.10 for both the Gamma-Theta and Intermittency transition model.

For both transition models it can be observed that transition differs significantly from the employed correlations. The most outstanding differences between the CFD simulations and the employed correlations are the onset to transition as well as the length of it. While the flat-plate correlations predict a short laminar region as well as a fast transition, the simulations predict a much longer laminar region and a slowest transition to turbulence.

In addition, all correlations lead to average heat transfer coefficients that are ± 20 % in comparison to the average heat transfer coefficient obtained from the CFD simulations. Moreover, and as it was theoretically expected for air, the n value that leads to better correspondence between simulations and correlations is $n = 0.4$ [24].

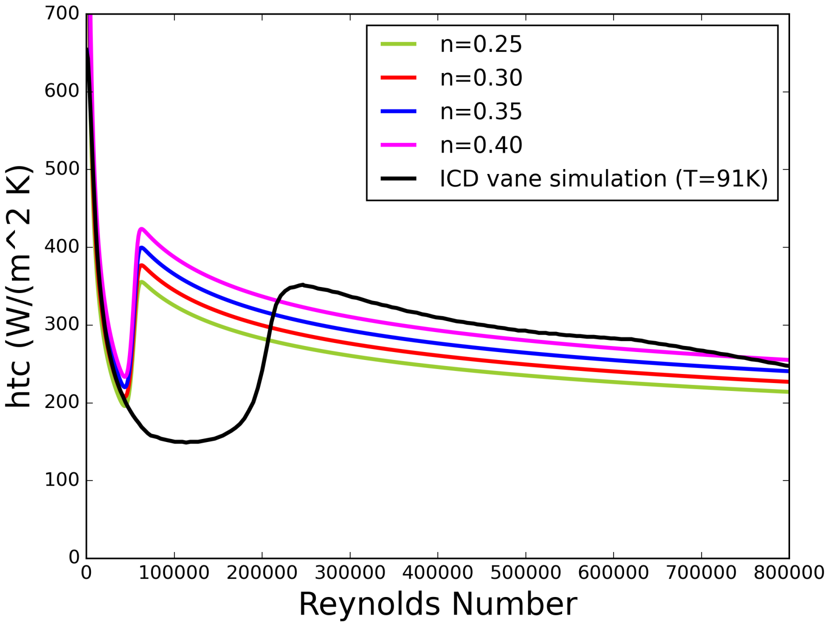

Figure 4.9: Comparison between the htc behaviour between the flat plate correlations and the CFD results for the Gamma-Theta transition model

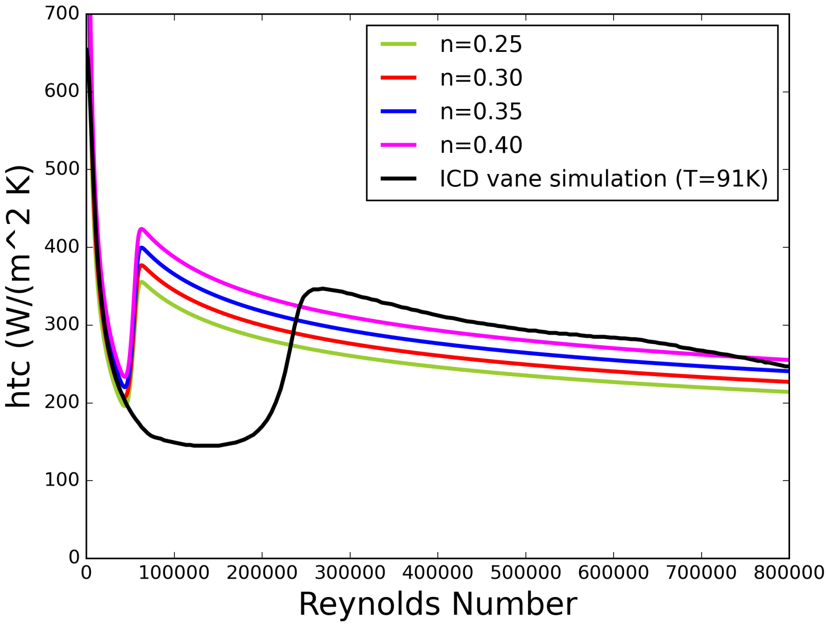

Figure 4.10: Comparison between the htc behaviour between the flat plate correlations and the CFD results for the Intermittency transition model

5

Conclusion

This project was carried out with the goal of reaching how to model the vane surfaces of an ICD so that cryogenic hydrogen is heated without incurring on additional pressure losses. To do so, two different CFD transition models, the Gamma-Theta and Intermittency models, were used with several different heat transfer boundary conditions so that the transition in an ICD was modeled.

Firstly, a mesh independence study was developed. From it, it was concluded that a well-refined mesh is needed to obtain appropriate results convergence. Reaching good convergence, was highly challenging due to the relatively small amount of heat being transferred along the vane in comparison to the enthalpy flow in the inlet and outlets of the ICD. Moreover, the mesh study also showed that both the onset and size of the transition region are mesh dependent. As a result, finer meshes lead to more delayed and prolonged transition regions than rough meshes.

Secondly, a parametric study was carried out with the goal of analyzing the effect of either cooling or heating on transition. To do so, different vane temperatures were defined. As a result, the theoretically expected fact that decreasing wall temperature leads to further downstream onsets as well as to longer transition zones, was proven.

Finally, a theoretical validation of the results was conducted based on flat plate correlations. However, for the two employed transition models, the flat plate correlations did not accurately predict the transition from laminar to turbulent regime. Indeed, the onset Reynolds number, which is one of the most relevant parameters in transition and that only depends on turbulence intensity and not on fluid properties, was smaller for the correlation cases than for the simulations. This may be linked to the fact that the turbulence intensity employed for the correlations is the one at the inlet of the ICD (4.8%) which may be slightly different from the one employed at the simulations, that is the one at the ICD vane.

In this project, the vane has been considered to be the only aerodynamic surface employed for heat transfer needs. However, taking into account new surfaces such as the the hub and shroud could be further investigated.

Moreover, in this project, the heat transfer process has been modelled considering warm water circulating inside the vane heating it and thereby, providing warm heat flux to the outside colder flow. However, using the ICD as a heat exchanger is ultimately intended to heat the hydrogen before going into the combustion chamber so that the global efficiency of the engine is increased and emissions are reduced. Thus, it is important to carry out new projects in where the heat transfer process using hydrogen is analyzed.

Up to this point, the theoretical accuracy and suitability of the gamma-theta and the intermittency transition model has been studied. However, it is of great importance to validate results with real-life behaviour. Therefore, future research can be developed in the Chalmers´s low pressure compressor rig with the aim of carrying out experimental and numerical validation of the analyzed phenomenon.

.

Bibliography

[1] European Commission. *A European Green Deal | European Commission.* URL: https://ec.europa.eu/info/strategy/priorities-2019-2024/european-green-deal_en+ (visited on 02/07/2022).

[2] European Union. *PROGRESS IN WP2-Fuel System Heat Management.* URL: https://www.enableh2.eu/progress-in-wp2/ (visited on 02/07/2022).

[3] International Energy Agency. *Data and statistics-IEA.* URL: https://www.iea.org/data-and-statistics/data-browser?country=EU28&fuel=CO2%20emissions&indicator=CO2BySector (visited on 02/07/2022).

[4] European Commission. *Reducing emissions from aviation.* URL: https://ec.europa.eu/clima/eu-action/transport-emissions/reducing-emissions-aviation_en (visited on 02/07/2022).

[5] The New York Times. *Europe Plans Aggressive New Laws to Phase Out Fossil Fuels.* URL: https://www.nytimes.com/2021/07/13/climate/eu-border-carbon-tax.html (visited on 02/07/2022).

[6] Sabine Fuss et al. "Moving toward net-zero emissions requires new alliances for carbon dioxide removal". In: *One Earth* 3.2 (2020), pp. 145–149.

[7] Akshay Nag Srinath et al. "Thermal Management System Architecture for Hydrogen-Powered Propulsion Technologies: Practices, Thematic Clusters, System Architectures, Future Challenges, and Opportunities". In: *Energies* 15.1 (2022), p. 304.

[8] İlker Yılmaz et al. "Investigation of hydrogen usage in aviation industry". In: *Energy conversion and management* 63 (2012), pp. 63–69.

[9] G Corchero and JL Montanes. "An approach to the use of hydrogen for commercial aircraft engines". In: *Proceedings of the Institution of Mechanical Engineers, Part G: Journal of Aerospace Engineering* 219.1 (2005), pp. 35–44.

[10] Stephen Rondinelli, Roberto Sabatini, and Alessandro Giacomo Maria Gardi. *Challenges and benefits offered by liquid hydrogen fuels in commercial aviation.* Tech. rep. RMIT University, 2014.

[11] Heinz G Klug and Reinhard Faass. "CRYOPLANE: hydrogen fuelled aircraft—status and challenges". In: *Air & Space Europe* 3.3-4 (2001), pp. 252–254.

[12] Anthony J Colozza and Lisa Kohout. *Hydrogen storage for aircraft applications overview.* Tech. rep. 2002.

[13] Carlos Xisto, Isak Jonsson, and Tomas Grönstedt. *Synergies with heat management Conceptual Design of a Compressor Vane-HEX for LH 2 Aircraft Engine Applications Conventional duct Aggressive duct design.* 2020.

[14] Theodore L Bergman et al. *Fundamentals of heat and mass transfer.* John Wiley & Sons, 2011.

[15] John R Howell et al. *Thermal radiation heat transfer.* CRC press, 2020.

[16] Jonas Bredberg. "On the wall boundary condition for turbulence models". In: *Chalmers University of Technology, Department of Thermo and Fluid Dynamics. Internal Report 00/4. G oteborg* (2000), pp. 8–16.

[17] Hermann Schlichting and Joseph Kestin. *Boundary layer theory.* Vol. 121. Springer, 1961.

[18] *Stability of Laminar Flows and Transition to Turbulence - Lesson 2.* URL: `https://courses.ansys.com/index.php/courses/basics-of-turbulent-flows/lessons/stability-of-laminar-flows-and-transition-to-turbulence-lesson-2/` (visited on 05/13/2022).

[19] *Ansys CFX: Turbomachinery CFD Software.* URL: `https://www.ansys.com/products/fluids/ansys-cfx` (visited on 04/28/2022).

[20] *CFX-Solver Modeling Guide.* URL: `https://ansyshelp.ansys.com/account/secured?returnurl=/Views/Secured/corp/v221/en/cfx_solv/cfx_solv.html` (visited on 04/28/2022).

[21] Osborne Reynolds. "IV. On the dynamical theory of incompressible viscous fluids and the determination of the criterion". In: *Philosophical transactions of the royal society of london.(a.)* 186 (1895), pp. 123–164.

[22] *CFX-Solver Theory Guide.* URL: `https://ansyshelp.ansys.com/account/secured?returnurl=/Views/Secured/corp/v221/en/cfx_thry/cfx_thry.html` (visited on 05/02/2022).

[23] *Laminar vs. Turbulent – Nusselt Number.* URL: `https://www.nuclear-power.com/nuclear-engineering/heat-transfer/convection-convective-heat-transfer/laminar-vs-turbulent-nusselt-number/` (visited on 05/13/2022).

[24] John H Lienhard. "Heat transfer in flat-plate boundary layers: a correlation for laminar, transitional, and turbulent flow". In: *Journal of Heat Transfer* 142.6 (2020).

[25] Isak Jonsson et al. "Design of Chalmers new low-pressure compressor test facility for low-speed testing of cryo-engine applications". In: *Proceedings of European Conference on Turbomachinery Fluid dynamics.* Vol. 14. 2021.

[26] Isak Jonsson et al. "Design and Pre-Test Evaluation of a Low-Pressure Compressor Test Facility for Cryogenic Hydrogen Fuel Integration". In: *Turbo Expo: Power for Land, Sea, and Air.* Vol. 84904. American Society of Mechanical Engineers. 2021, V02AT31A022.

[27] Marcus Lejon et al. "Multidisciplinary design of a three stage high speed booster". In: *Turbo Expo: Power for Land, Sea, and Air.* Vol. 50794. American Society of Mechanical Engineers. 2017, V02BT41A037.

[28] *CFX-Pre User´s Guide.* URL: `https://ansyshelp.ansys.com/account/secured?returnurl=/Views/Secured/corp/v221/en/cfx_pre/cfx_pre.html%5C%23cfx_pre` (visited on 05/13/2022).

[29] Isak Jonsson. “Experimental Aerothermal Study of Internal Jet Engine Structures”. PhD thesis. Chalmers Tekniska Hogskola (Sweden), 2021.

[30] Vaclav Cyrus. “An Experimental Study of Stall in Four Axial Compressor Stages”. In: *Turbo Expo: Power for Land, Sea, and Air*. Vol. 78545. American Society of Mechanical Engineers. 2000, V001T03A073.

[31] *NIST Reference Fluid Thermodynamic and Transport Properties Database (REFPROP): Version 10*. URL: `https://www.nist.gov/srd/refprop` (visited on 05/29/2022).

DEPARTMENT OF MECHANICS AND MARITIME SCIENCES
CHALMERS UNIVERSITY OF TECHNOLOGY
Gothenburg, Sweden
www.chalmers.se